CHALMERS

Material Characterization and Machining Performance of Nodular Cast Iron

Investigating Variations in Graphite Morphology and Machinability Between and Within Components

Bachelor’s Degree Project within Mechanical Engineering

EMIL GRANUNG
ANGELICA WERNER

DEPARTMENT OF MECHANICAL ENGINEERING
DIVISION OF MATERIALS AND MANUFACTURE

CHALMERS UNIVERSITY OF TECHNOLOGY
Gothenburg, Sweden 2026
www.chalmers.se

Material Characterization and Machining Performance of Nodular Cast Iron

Investigating Variations in Graphite Morphology and Machinability Between and Within Components

Emil Granung

Angelica Werner

DEPARTMENT OF MECHANICAL ENGINEERING

Division of Materials and Manufacture

CHALMERS UNIVERSITY OF TECHNOLOGY

Gothenburg, Sweden 2026

Material Characterization and Machining Performance of Nodular Cast Iron

Investigating variations in Graphite Morphology and Machinability between and within Components

Emil Granung

Angelica Werner

Supervisor: Daniel Andersson, Department of Mechanical Engineering

Co-supervisor: Jonas Svensson, Volvo Trucks Technology & Industrial

Examiner: Peter Krajnik, Department of Mechanical Engineering

Bachelor Thesis 2026

Department of Mechanical Engineering

Division of Materials and Manufacture

Chalmers University of Technology

SE-412 96 Gothenburg

Telephone: 031-7721000

Abstract

The objective of this degree project was to investigate material and machining variations in nodular cast iron similar to EN-GJS-500-14, both between components from the same batch and within individual components. The aim was to examine the microstructure and properties of the material, as well as analyze the results of cutting tests, in order to minimize cutting tool consumption. To investigate the material variations, several analyses were performed, including preparation of samples, from which optical microscope images were acquired to analyze differences in graphite particles. Furthermore, some samples were etched to reveal the microstructure, after which hardness testing was performed. To evaluate machining performance, cutting tests were conducted using a turning machine. Tool wear and cutting forces were investigated, and scanning electron microscope (SEM) images of the cutting tools were taken to further analyze tool wear and material adhesion on the tool surface.

Differences in graphite particles were observed across different axial positions within the same component, with higher values recorded along the edges compared to the central sections. Measured values included nodularity, particle density, and particle shape and size distribution. Cooling rate could explain all these variations as the major differences are evident along the outer edges and within thin sections of the components. The etched samples mainly consisted of ferrite, and the hardness of the samples corresponded to the nodularity. In machining, variations were also detected, where the maximum flank wear correlated with the nodularity and hardness of the material. Additionally, an increase in the resultant force showed similar correlation. SEM images revealed that the wear had not yet reached the cemented carbide and showed significant amounts of adhered material on the substrate.

Keywords: Nodular Cast Iron, Nodularity, Tool Wear, Graphite Particle, Machining

Acknowledgements

This bachelor's degree project, corresponding to 15 credits (HP), was carried out during spring 2026 as the final examination of the Bachelor's Program in Mechanical Engineering at Chalmers University of Technology.

The work was performed at the division of Materials and Manufacture at Chalmers University of Technology, and we would like to express our gratitude to everyone who contributed to this project.

First, we would like to thank everyone at CentreX for the support in making this opportunity possible and the encouragement during the entire project. We would also like to thank Volvo Truck Technology & Industrial for providing the wheel hubs, with a special gratitude to our co-supervisor Jonas Svensson and Oskar Bohlin for their insights and support.

We would also like to thank our examiner at Chalmers, Peter Krajnik, for the academic insights and helping us complete this project for our Bachelor's degree.

Finally, a special acknowledgment is dedicated to our supervisor, Daniel Andersson, for his valuable commitment, guidance and knowledge throughout the entire project. His insights and patience have been essential for the completion of this work, and we are deeply grateful for the support provided.

Emil Granung & Angelica Werner, Gothenburg, Sweden, June 2026

Table of Contents

1. Introduction

The adaptable characteristics of cast iron create an in-demand material that is widely used across different industries (Buschow et al., 2001). To be competitive in the automotive industry, the need for economically viable and reliable materials that meets the operational requirements of vehicles increases every year (Orłowicz et al., 2015). Using metal casting, due to its economically beneficial use of material and possibility to adhere to complex geometries, it becomes advantageous for applications in automotive, defense and aerospace markets (Huda, 2025).

However, in today's cast iron industry, it is difficult to predict the material and mechanical properties of nodular cast iron components. This uncertainty mainly arises during the casting process and affects tool wear during machining operations. It is not only differences between similar components within the same production batch, but also within the same component (D. Andersson & A. Malakizadi, 2025). As a result, tool life becomes hard to predict. Instead of machining based on the actual material properties of each component, machining parameters are selected according to the worst-case conditions. Therefore, cutting tools are not utilized to their full potential, leading to excessive tool consumption, resulting in unnecessarily high production costs.

There are several different types of cast iron, including white, gray, compact graphite and nodular cast iron. Nodular cast iron is mainly used in applications due to its favorable mechanical properties, such as high fatigue resistance. Its rounded graphite particles also promote high ductility and strength, which makes the material suitable for a wide range of applications (de Sousa et al., 2017). The material and mechanical properties of nodular cast iron, as well as tool wear, is a broad subject investigated in several ways. While studies on machining of cast iron in general are more common, the properties of nodular cast iron used in a specific component, and its effect on tool wear, is limited.

Nodular cast iron has become an advantageous material that is applicable on several different automotive components. With the automotive industry being more competitive, the need for reducing costs is more evident than ever. Using real life components and material from the industry, further investigation into the variability of nodular cast iron between and within components is intriguing to help solve the challenges of using tools to their full potential.

1.1 Study Motivation and Context

The expected outcome of this degree project is an increased understanding of the material and machinability variability in metal cutting, specifically the wheel hubs provided by Volvo. This contributes to the purpose of investigating the mechanical properties of nodular cast iron. Key factors influencing the machinability of the studied material will be identified, leading to a more comprehensive understanding of the material and with further studies be able to improve prediction of cutting tool lifespan during machining operations.

The project includes identifying variations in material properties both between different components and within the individual component, including measuring nodularity, graphite particle density, graphite size and hardness. Furthermore, the effect of these material variations on machining responses is investigated, with the aim of establishing correlations between material variability and machining performance.

1.2 Aim

The project aims to investigate material characteristics of nodular cast iron, as well as their effect on machining responses. This will be executed by sampling different positions on wheel hubs provided by Volvo, along with studying the machinability of the material.

1.3 Limitations

The subject of material characteristics and machining responses of nodular cast iron is broad and includes multiple features that can be considered. To achieve a structured and reliable analysis, the project will center exclusively on nodular cast iron of three wheel hubs provided by Volvo, all from the same batch. The material variation between and within components can then be compared and analyzed with high precision.

There are multiple material characteristics of nodular cast iron affecting its performance. Given the time frame of this degree project, the project will specifically study graphite properties, including nodularity, particle density, shape and size distribution, microstructure and hardness. Graphite properties and microstructure are analyzed using images of optical microscopy.

Machining processes can also be researched on different levels and with different aspects. The primary focus of the project will be on tool wear, using optical microscopy and scanning electron microscopy (SEM), and cutting forces, based on data collection from a dynamometer during turning. The optical microscopy will specify on measuring flank wear. SEM analysis of tool wear is planned to provide a detailed overview of the cutting tools.

1.4 Research Questions

Following research questions are to be studied:

- What are the material characteristics of the provided material?
  - What graphite properties variations within one component are there?
  - What graphite properties variations between components are there?
  - How are the material microstructure and hardness?
- Is the tool wear correlated with the cutting forces?
- How are the tool wear and cutting forces affected by different graphite properties and hardness?

2. Background

Metal casting started long before the industrial revolution and is still one of the most used processes to create complex shapes because of its versatility and applicability on any meltable metal (ASM International, 1988). Due to its economically beneficial use of material and possibility to adhere to complex geometries it is advantageous for applications in different industries (Huda, 2025).

Molten metal is poured into a mold corresponding to the negative geometry of the desired shape. The two most used casting methods for cast iron are sand casting and investment casting, with sand casting being the most common (Manek Casting, 2024). During casting, different parts of the component have different cooling rates, depending on the mold design, the local geometry thickness, and how the mold is filled. These variations in cooling rate leads to microstructure variations, which can significantly affect the mechanical properties of the material (Sild, 2024).

2.1 Cast Iron

Cast iron is a material widely used in industry due to its desirable characteristics, such as durability, strength and thermal stability, as well as its versatility, due to the ability to produce complex shapes to a lower cost (de Sousa et al., 2017). It primarily contains iron, carbon and silicon, and in many cases sulfur, manganese and phosphorus are added to modify the properties of the cast iron. Carbon and silicon are the materials that influence the microstructure the most in cast irons (U.S. General Services Administration, 2016). By adding carbon, the amount of graphite particles is adjusted, and the silicon works as a graphitizing element that promotes the decomposition of iron carbide (de Sousa et al., 2017).

Cast irons generally have the material properties of being hard, brittle and is more fusible than steel (U.S. General Services Administration, 2016). The high carbon content in cast irons makes the melting temperature relatively low (Hiratsuka, 2022). One of the main advantages is its ability to easily be shaped by casting, which is utilized in combustion engine blocks and heads. Another advantage is its vibration damping capacity, making it appropriate for components that are exposed to significant vibrations (de Sousa et al., 2017).

There are four primary types of cast iron: white, gray, compact graphite and nodular. Each type has its own advantages and drawbacks that make it suitable for different applications. Table 2.1 presents the properties of the different cast irons and is based on the work of de Sousa et al.

(2017), Modulus Metal (n.d.) and Penticton Foundry (2016). These will be described more in depth in the following sections.

***Table 2.1**: Properties of Cast Irons*

Type / Property	White	Gray	Compact Graphite Cast Iron (CGI)	Nodular
Ultimate tensile strength (MPa)	350	235	500	650
Hardness (HB)	470	200	225	270
Young modulus (GPa)	175	110	140	165
Fatigue resistance (MPa)	140	100	205	265
Thermal conductivity (W/mK)	23	48	35	28

2.1.1 White Cast Iron

For white cast iron, all the carbon presents itself as cementite or other carbides (de Sousa et al., 2017). The microstructure of white cast irons consists primarily of large regions of cementite together with pearlite. White cast iron is produced when carbon is prevented from forming graphite, using mainly chromium, as the metal solidifies. This makes the material hard, brittle and difficult to machine, while also giving the white cast iron its bright appearance (Singh, 2016b; ASM International, 1988). These cast irons are abrasion-resistant and generally considered to be unweldable (ASM International, 1988). Machining white cast iron requires cutting fluid with good coolant ability due to high heat generation (de Sousa et al., 2017).

2.1.2 Gray Cast Iron

In gray cast irons, the graphite is in the form of flakes or lamellae (de Sousa et al., 2017). Silicon combined with the slow cooling rates promote the graphitization in the iron. The matrix can vary from ferrite to pearlite, including mixed ferrite-pearlite structures (ASM International, 1988). The graphite flakes make the material softer, easier to machine and less brittle compared to white cast irons (de Sousa et al., 2017). Gray cast iron exhibits a compressive strength that is approximately three to four times stronger than its tensile strength due to its graphite flakes. Under compressive loads the flakes are pressed together, whereas under tensile loads they act as stress concentrators, initiating cracks more easily (ASM International, 1988). Large graphite flakes negatively affect the strength and ductility of gray cast iron, so inoculants are used to create finer and more numerous flakes (Singh, 2016a). The presence of graphite flakes gives gray cast iron high thermal conductivity and wear resistance, which makes the material suitable for components exposed to cyclic thermal loads, such as brake discs, engine blocks, and cylinder heads. Furthermore, due to the flake-shape graphite stress is concentrated more effectively in the main deformation zone during metal cutting, leading to easier cutting (de Sousa et al., 2017).

2.1.3 Compact Graphite Cast Iron (CGI)

The graphite in compact graphite cast irons is vermicular, which is a hybrid form between flake and nodule graphite. It is elongated and randomly oriented, similar to gray cast iron, but the particles are shorter, thicker, and have rounded ends compared to graphite flakes (de Sousa et al., 2017). These shape characteristics usually results in a nodularity of 25% (Rundman, 2001). To obtain vermicular graphite, the graphite is partly nodularized by adding a small amount of magnesium (0,01-0,02%) to the melt. The morphology of compact graphite cast iron, mainly its graphite shape, inhibits crack propagation. Furthermore, the graphite structure promotes strong adhesion between the graphite and the metallic matrix, which may consist of pearlite, ferrite, or a combination of both. Compared with gray cast iron, the material offers improved mechanical strength, ductility and toughness, but lower thermal conductivity, vibration absorption and machinability (de Sousa et al., 2017). When machining compact graphite cast iron, similar problems to those encountered with white cast iron may arise due to significant heat generation, making cutting fluid necessary during continuous machining (Nayyar et al., 2012).

2.1.4 Nodular Cast Iron

Nodular cast iron, also known as ductile iron or spheroidal graphite cast iron (SGI), contain graphite particles of nodular form. It is produced by alloying a small amount of magnesium to the silicon alloyed cast iron to create nodular graphite particles. The amount of added magnesium alloy must be between 0,03% to 0,05% to create the nodular particles since other magnesium ratios generate other shapes, decreasing the ductility (Buschow et al., 2001).

The nodular graphite particles generate a fracture toughness up to six times higher than for the particles of gray cast iron (Buschow et al., 2001). This increased fracture toughness in nodular cast iron is based on the change in fracture propagation caused by the graphite particles in the material. Cracks in cast iron mainly propagate through the graphite particles, as the surrounding matrix is much tougher, making the graphite act like a notch. The nodular particles lower stress concentrations and act as hindrances for crack propagation, in turn improving the ductility, hardness and tensile strength of the material (ASM International, 1988; International Organization for Standardization, 2006). This makes nodular cast iron suitable for parts that are exposed to high mechanical stress (Mori et al., 2025).

The low stress concentrations make machining less effective, as the cutting is not assisted by crack propagation. This, together with the higher mechanical properties, leads to increased cutting forces (de Sousa et al., 2017; Ren et al., 2019). The addition of elements such as copper and nickel can improve the machinability of nodular cast iron, as they help to reduce cutting forces and surface roughness (de Sousa et al., 2017).

2.1.5 Nodularity

Material characteristics of cast iron are often measured using four standards from International Organization of Standardization, which focuses on the microstructure of cast irons. For nodular cast iron, ISO 945-4:2019 specifically addresses nodularity due to the nodular graphite particles importance for mechanical and physical properties. Nodularity measures the percentage of graphite particles that meet the predetermined size and roundness criteria (International Organization for Standardization [ISO], 2019b).

The nodularity is therefore dependent on the graphite particles size and shape. Apart from the amount of magnesium alloyed into the material, the graphite particles are also affected by the rate of cooling. The longer the solidification time, the more the nodularity is reduced as well as the particle count. For a slower cooling rate, the size of the particles increases while also becoming chunkier. While nodularity is dependent on graphite particles, the graphite particles also influence the material. For example, the hardness of the material (Di Egidio et al., 2025).

2.1.6 Microstructure of Cast Iron

The microstructure of the cast iron significantly affects its mechanical properties. Phases in cast iron microstructure include ferrite, cementite and pearlite. The properties of these phases are summarized in Table 2.2, based on ASM International (1988), Luque et al. (2010) and Yuantai Steel Pipe (2024):

Table 2.2*: Properties of Ferrite, Cementite & Pearlite*

Phase / Property	Ferrite	Cementite	Pearlite
Tensile strength (MPa)	280	3000–6000	862
Elongation (%)	61	≈1	10
Hardness (HB)	75	550	200

The ferrite matrix is the soft α-iron phase containing a small amount of carbon, with a maximum of 0,02 wt% carbon at 723°C (Hiratsuka, 2022). Ferrite has low tensile strength but exhibits high ductility and is easily machined. The addition of graphitizers, for example silicon, combined with using slow cooling rates, promotes ferrite formation (ASM International, 1988). Ferrite has a body-centered cubic (BCC) crystal structure, which contributes to its ductility, but only allows small amounts of carbon to be dissolved in the lattice (Hiratsuka, 2022; Nuclear Power, n.d.).

Cementite is a chemical compound of iron and carbon, commonly classified as a ceramic in its pure form, resulting in a hard and brittle phase. It consists of three iron atoms and a carbon atom in a rhombic crystal structure, corresponding to 6,67 wt% carbon (Nuclear Power, n.d.; Sabner, n.d.; Hiratsuka, 2022). Its formation is promoted in regions of a casting that cool rapidly, such as thin sections, corners, and near the surface. When the carbon equivalent is low, particularly in iron with low silicon levels, the structure is more prone to form cementite rather than graphite (ASM International, 1988).

Pearlite is a microstructure consisting of ferrite and cementite arranged in alternating lamellar layers, containing 87,5 wt% ferrite and 12,5 wt% cementite (Hiratsuka, 2022). Compared to ferrite, pearlite exhibits higher tensile strength and hardness, but lower ductility. The mechanical properties of pearlite are determined by the distance between the lamellar layers. As the space between the layers decreases, hardness and tensile strength increases. Finer pearlite can be achieved through rapid cooling rates or alloying (ASM International, 1988).

2.2 Turning

The following section presents different turning operations, as well as cutting forces and common cutting parameters relevant for this machining process. This chapter also covers the materials and coatings commonly used in cutting tools, focusing on cemented carbide and CVD coatings. In addition, the definition of tool wear and its different types are discussed, with the main emphasis on flank wear.

2.2.1 Turning Operations

Turning is a common machining process that removes material from a rotating workpiece using a cutting tool. The process is performed on a lathe and operates in two axes, Z-axis for axial movement along the center of the workpiece and radially with the X-axis (Meyers & Slattery, 2001). The most common turning operations are longitudinal-, profile- and face turning.

Longitudinal turning reduces the diameter of the workpiece by removing material parallel to the Z-axis. Similar to longitudinal turning, the profile turning removes material along the Z-axis while simultaneously varying the position in the X-axis, creating different diameters over the workpiece. The changing depth and speed will however increase the stress and requirements on the tool. When reducing material radially, the tool is fed along the X-axis towards the center of the workpiece and this is called face turning. Face turning thereby uses the tool to reduce the length of the workpiece, hence requiring higher radial cutting forces (Sandvik Coromant, n.d.b).

2.2.2 Cutting Forces

Cutting forces are important measurements in machining and their magnitudes are dependent on both the type of tool used as well as the material. These forces are commonly measured using a dynamometer connected to the tool, which measures forces in three directions (Trent et al., 2025). However, the force components are defined differently depending on the turning operation (ISCAR, n.d.). Face turning has three forces: cutting force, feed force and passive force. Cutting force (F_c) is applied in the same direction as the cutting velocity. The force acting parallel to, but in opposite direction of the feed motion is called Feed force (F_f) and the axis for this force is exchanged with the passive force in longitudinal turning. Lastly, the smallest force is often the Passive force (F_p) and it is applied in a direction pushing away from the workpiece (Trent et al., 2025). From these force components, the resultant force is determined as their vector sum (Kistler, n.d.). All forces and directions for face turning are illustrated in Figure 2.1.

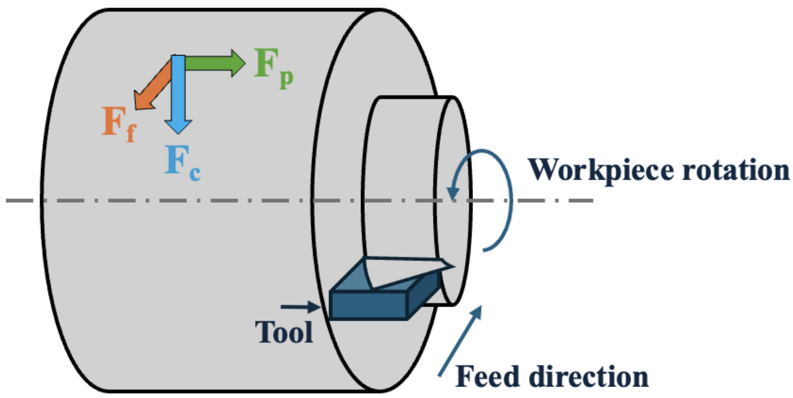

Figure 2.1: *Illustration of acting forces within face turning*

2.2.3 Cutting Parameters

Cutting forces should be reduced to minimize the stress on the tool and lower the effort required to remove material. The cutting forces are affected by several parameters simultaneously, e.g: feed rate, cutting speed and cutting depth (Rao et al., 2013). They are also affected by factors such as workpiece material and the use of cutting fluids (Denkena et al., 2021; El-Hofy, 2013). Feed rate (f) is mostly referred to in mm/rev (millimeters per revolution) and can be described as the distance the tool advances per revolution (Trent et al., 2025). Setting the feed rate too low influence flank wear and built-up edge negatively, while also leading to higher production costs due to increased machining. A too high tool feed negatively affects chip control, crater wear and surface finish (Sandvik Coromant, n.d.c). Cutting speed (V_c) uses the unit m/min (meter per minute) and refers to the speed of the workpiece rotation (Trent et al., 2025). A low cutting speed promotes built-up edge, higher manufacturing costs and poor surface. In contrast, too high cutting speed results in poor finish, accelerated flank wear and plastic deformation (Sandvik Coromant, n.d.c). Cutting depth (a_p) is the thickness of material removed measured in millimeters (Trent et al., 2025). Smaller cutting depths causes vibration and less chip control, while too deep cuts require higher power consumption and increased cutting forces (Sandvik Coromant, n.d.c).

2.2.4 Cutting Tool Material

Cutting tool materials are selected based on the type of operation being performed. Influencing factors include the material to be machined, the type and form of the component, machining conditions, and the required surface finish. All cutting tools for turning consist of a substrate, for example cemented carbide, ceramic, cubic boron nitride, or diamond. Many tools also feature coatings that enhance durability and cutting performance. The combination of substrate and coatings determines the hardness, toughness, and wear resistance of the tool (Sandvik Coromant, n.d.a).

Cemented carbide is a composite of tungsten carbide (WC) particles with cobalt (Co) as the binder material, typically containing more than 80% tungsten carbide. The tools are manufactured either by powder pressing or injection molding techniques, followed by sintering (Sandvik Coromant, n.d.a). Sintering is a process in which the tool is heated to a temperature of 1100-1300°C, causing metal particles to bond together (ESMA, n.d.). The tungsten carbide grain size is the most important factor in determining the hardness-toughness balance. A smaller grain size results in a greater hardness for a given amount of binder. Furthermore, the amount of cobalt relative to tungsten carbide controls the toughness and resistance to plastic deformation in the material. Therefore, an increased cobalt content leads to a tougher material, while a lower content results in more brittle characteristics (Sandvik Coromant, n.d.a).

There are two main methods for depositing a coating on a cemented carbide substrate: Chemical Vapor Deposition (CVD) and Physical Vapor Deposition (PVD). PVD creates thinner coatings that are more suited for fine processing and finishing applications. A CVD coating is formed through chemical reactions and is characterized by high wear resistance and excellent adhesion to cemented carbide. These CVD coatings can be deposited either as a single layer or multiple layers, with different materials selected according to the desired properties of the tool. A common type of CVD coating consists of a combination of titanium carbonitride (TiCN), aluminum oxide (Al_2O_3) and titanium nitride (TiN). Titanium carbonitride enhances abrasive wear resistance, which leads to reduced flank wear. Aluminum oxide enhance the resistance to plastic deformation, while also reducing crater wear with its low thermal conductivity. Titanium nitride is used for improving wear resistance and for detecting wear (Sandvik Coromant, n.d.a).

2.2.5 Tool Wear

Tool wear is the progressive loss of material from a cutting tool due to its interaction with the workpiece. Such wear can be a result of mechanical, thermal, and chemical interactions (Shenzhen Tuofa Technology, 2025). A worn tool can have several effects on the machining. For example, lower cutting-edge sharpness decreases the effectiveness of material removal, resulting in a lower surface finish quality. Increased tool wear also leads to higher cutting forces, as more force is required to remove material with a worn tool. Additionally, it can affect the tool geometry, causing the final component to deviate from the desired shape. Furthermore, tool wear affects cutting performance, resulting in longer cycle times, lower cutting speed, and reduced productivity (Acharya, 2023). Therefore, cutting tools must be replaced before they become excessively worn. However, a short tool life requires frequent tool changes, which can be time consuming. This could be fixed by reducing the cutting speed, but this also leads to longer cycle times. The optimal approach is to select a better tool or modify the workpiece material to enhance machining (HN Carbide, n.d.).

There are different types of tool wear, including flank wear, crater wear, built-up edge, notch wear, plastic deformation, and thermal cracks. Flank wear is the most frequently encountered type. It occurs on the flank face of the tool and is mainly caused by abrasion due to hard constituents within the workpiece material, as illustrated in Figure 2.2 (Sandvik Coromant, n.d.d). Consequently, flank wear often correlates with the hardness of the workpiece material, where machining harder materials generally result in increased flank wear (Senthilkumar et al., 2014). It can also be caused by diffusion wear at high cutting speeds, due to higher temperatures. To reduce flank wear, the cutting speed can be lowered, a more wear resistant material can be chosen, and coolant can be used efficiently (Seco Tools, n.d.). Flank wear is measured from the cutting edge to the wear end on the flank (TechMet, n.d.). The limits, commonly used in practice, for replacing a cutting tool are an average flank wear width of VB_B=0,3 mm and a single point maximum width of VB_{max}=0,6 mm (Daicu & Oancea, 2022).

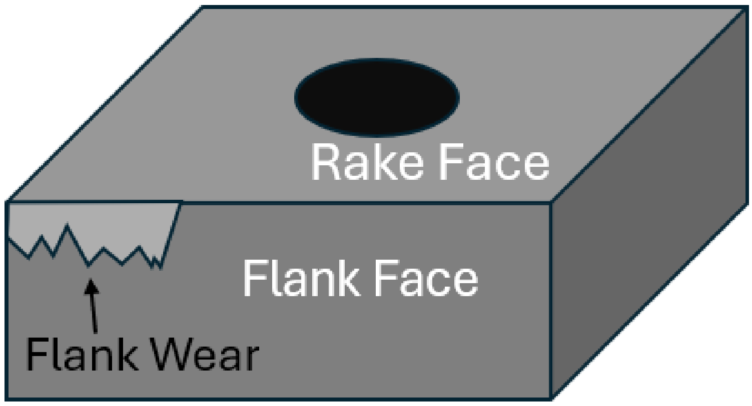

***Figure 2.2**: Schematic illustration of a cutting tool with flank wear*

Measuring tool wear in turning can be performed over time (tool life) or by using Spiral Cutting Length (SCL). Tool life refers to the time it takes for a tool to become unusable by a predetermined criterion (Klocke, 2011). Alternatively, SCL uses a predetermined length for the tool to be used in the machining process. It refers to the total chip length generated during machining and can be viewed as a preferable method of analyzing tool wear. The advantages of SCL, compared to tool life tests, are predictability of time and material consumption as well as the ability to analyze tool wear at any given time (Andersson & Aronsson, 2024).

2.3 Machinability

Machinability can be described by how easily a material can be removed from a workpiece with an acceptable surface quality. Materials with good machinability have several advantages, such as reduced cutting forces, the ability to machine at higher cutting speeds, improved surface quality, and reduced tool wear compared to materials with poor machinability. However, enhancing material performance properties often comes at the expense of machinability, making it necessary to find an appropriate balance (El-Hofy, 2013). Machinability does not only depend on the material, but also on the machining system and its configuration. There are four main factors commonly used to evaluate machinability, where tool wear and the significance of the forces are two factors. The third factor, chip formation, is evaluated based on chip breakability and how easily the chips are transported from the cutting zone. Surface roughness is the final factor measured (Astakhov, 2014).

2.4 Scanning Electron Microscopy

Scanning electron microscopy (SEM) is a technique used to generate high-resolution images using a concentrated beam of electrons to scan the surface of a sample inside a vacuum chamber. The microscopy sends out multiple beams with electrons to interact with the atoms within the sample to create an image. This method results in a significantly higher resolution compared to optical microscopy (Nanoscience Instruments, n.d.).

There are two main types of signals generated by the interaction between the electron beam and the sample surface: secondary electrons and backscattered electrons. Secondary electrons are produced when the electron beams interact with the sample through inelastic scattering process. These electrons are emitted from the surface region and provide high-resolution images of the surface topography. Backscattered electrons, on the other hand, arise from elastic interactions and present more detailed information about the material composition of the sample. This method develops an image highly dependent on the atomic number of the material. Areas with higher atomic numbers appear brighter in the image, while regions with lower atomic numbers appear darker (Thermo Fisher Scientific, n.d.).

3. Methodology

The methodology for this project is divided into three main parts: literature review, material characterization and metal cutting. Three wheel hubs, see Figure 3.1, made of nodular cast iron (NGI) were provided by Volvo Trucks Technology and Industrial for this study and are referred to in this degree project as wheel hub A, B and C. The nodular cast iron used in the wheel hubs was similar to EN-GJS-500-14.

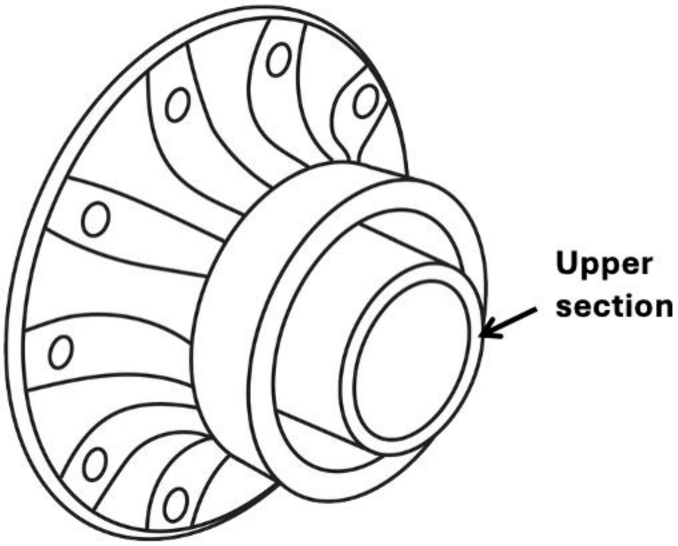

***Figure 3.1**: Illustration of provided wheel hub*

3.1 Literature Review

Using primarily the databases provided by Chalmers library and Google scholar, the project aims to use a literature review with information gathering from relevant literature sources as well as different measurement techniques. Mainly primary literature sources are to be used to avoid misinterpretations and biases as well as data collection directly from the tests and samples conducted. Secondary literature resources are, however, to be used when the primary source is in a foreign language.

As previous research lays the groundwork for the project, information about cast irons, with a focus on nodular cast iron was gathered and analyzed. The purpose was to establish theoretical knowledge before experimental work and tests were conducted, while also acting as supporting documents during the entire scope of the project. Initial literature covers cast irons in general, providing an overview of the different types of irons and their characteristics. This includes, but is not limited to, the graphite particles and the mechanical properties. In addition, the influence of cutting parameters on tool performance is reviewed along with literature describing the operations performed in the project.

3.2 Material Characterization

The wheel hubs were examined in several different steps to characterize the material. First, sample preparation was performed to enable microscope examination on the wheel hubs. An optical microscope was used to acquire images of the sample surfaces. Subsequently, a Python script was created to analyze the images, determining the preselected graphite properties. The samples were then etched to reveal the microstructure, before hardness testing was carried out.

3.2.1 Sample Preparation

The first section selected for sample preparation was the flange from Volvo's wheel hub B, as shown in Figure 3.2 and was cut using a metal cutting band saw. Subsequently, the same band saw was used to extract the samples. These samples are referred to as F1 to F4 and were extracted to investigate variations within different regions of the same component. The samples investigated differed in wall thickness and location in the geometry to study the effect it would have on the graphite properties. F1 had a small wall thickness while sample F2 was cut to examine the effect the distance to the edge has on the graphite. The last two samples were taken close to the flange hole to analyze the graphite in that area as well as a thicker wall. The location of all four samples is illustrated in Figure 3.3. The arrows indicate the surfaces examined, while the dashed lines show the samples original position.

Figure 3.2*: Outer structure of the wheel hub*

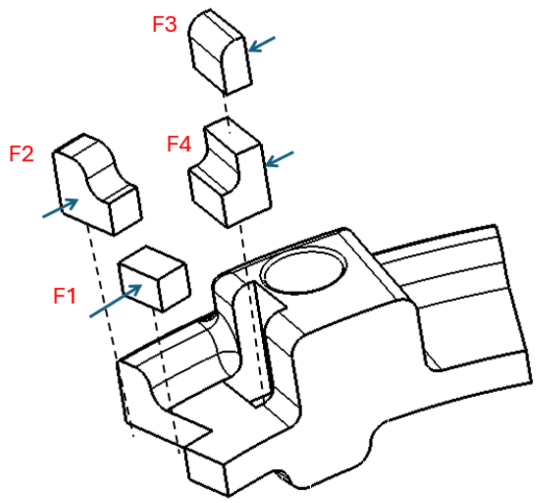

Figure 3.3*: Schematic view of flange samples from wheel hub B*

The second section examined was a pipe geometry from wheel hub A initially cut into three circular sections: upper, middle, and lower, using a band saw. Thereafter, each section was further cut into smaller samples, also using a band saw. Sample P1 was taken from the upper section, samples P2 to P5 from the middle section, and sample P6 from the lower section, as illustrated in Figure 3.4. Samples P1, P2 and P6 were located on the same parting line of the cast hub. Additionally, two samples were obtained from previously turned pipes: sample P7 and sample P8 from wheel hub B and C, respectively. These samples were taken from the exact same location as the middle section in wheel hub A. The main purpose of samples P1 to P8 was to investigate whether there were variations within the same component depending on location, as well as to determine if differences exist between different workpieces.

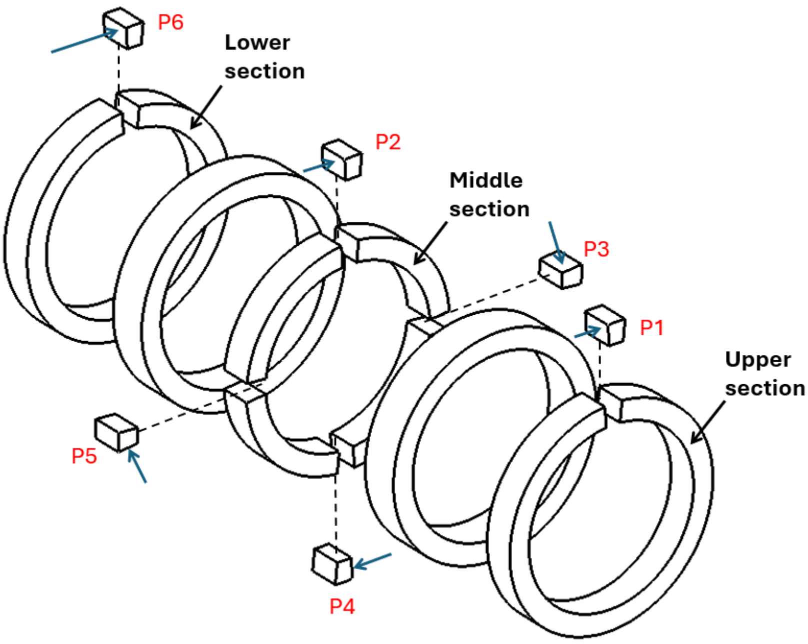

Figure 3.4: *Schematic view of the pipe from wheel hub A, including the cut-out samples*

Following the cutting process, the samples were mounted. Molds with a diameter of 30 mm were used for the flange samples, while molds with a diameter of 40 mm were used for the samples from the pipe. The larger molds were selected to fit the entire sample without the risk of the mold breaking, as these samples were larger. A conductive resin (PolyFast) was selected as the mounting material for the samples to enable SEM analysis. After mounting, both batches of samples were prepared in the same way. First, a Struers Abrapol-2 grinding machine was used. This machine applied pressure to the sample holder rather than an individual sample. When using this sample holder, the samples must be fixed with threaded rods. A hex key was used to ensure that the samples were fixed in place. Grinding and polishing were performed in four steps: two grinding steps followed by two polishing steps. For each step 150 rpm was used and Table 3.1 presents the remaining parameters:

Table 3.1 *: Grinding and polishing steps*

Step \ Parameter	Surface	Lubricant/Suspension	Force / Sample [N]	Time [min]
1	SiC-paper 220#	Water	25	2
2	MD-Largo	DiaPro Allegro/Largo (9 micro)	25	5
3	MD-Dac	DiaPro Dac (3 micro)	25	4
4	MD-Nap	DiaPro Nap B (1 micro)	15	2

Between each step, the samples were cleaned. For step 1, the samples were rinsed with water and then dried using cotton. This was followed by ethanol cleaning and compressed air drying. The air drying was performed carefully to prevent particles from damaging the surface. During steps 2 to 4, the suspension was applied in a sufficient amount to ensure proper polishing of the surface. After each of the next steps, ethanol was used for cleaning. The ethanol was applied immediately after grinding and polishing to prevent the sample surface from oxidating. Thereafter, the surfaces were dried with cotton, followed by a second ethanol rinse and compressed air. As a final cleaning step, the samples were placed in an ultrasonic cleaner to remove particles and contaminants from the surface.

After completion of these steps, the samples were ready for examination. Figure 3.5 shows an image of a prepared sample.

Figure 3.5*: Image of a prepared sample*

3.2.2 Optical Microscopy

All samples were examined using an optical microscope, specifically a Zeiss Axioscope 7, to observe differences in their graphite morphology. For each sample, one stitched image showing the entire sample surface was captured to identify any trends that required further investigation.

Following this, ten images were taken from each sample at 10X magnification to analyze the graphite particles. These images were later used in a Python code developed for the image analysis, as described in chapter 3.2.3. To obtain an accurate representation of each sample, the images were captured within a central region, illustrated by the dashed square in Figure 3.6.

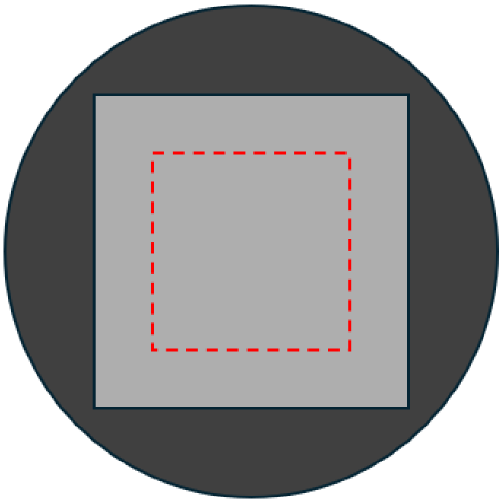

***Figure 3.6**: Illustration of the selected central region for image acquisition*

Images were intentionally not collected near the edges of the samples, as the overview images indicated that the graphite near the edges exhibited a more flake shaped graphite rather than a nodular shape. These regions were therefore considered not to represent the overall sample and thus excluded from the analysis. Ten images at 10X were considered sufficient, as the graphite count exceeded the minimum requirement of 500 particles and the minimum number of observation areas, which is five, according to International Organization for Standardization (2019b).

3.2.3 Python Script - Nodularity

A Python script was created to analyze the images taken by the optical microscope. The script distinguished between the black graphite and the white background to identify all graphite particles. Particles connected to the image frame were excluded from the analysis, as their full shape was impossible to determine. For each graphite particle, the script calculated the Féret diameter, by analyzing the particles outer boundary. The Féret diameter is defined as the maximum distance between two points within the particle, see Figure 3.7.

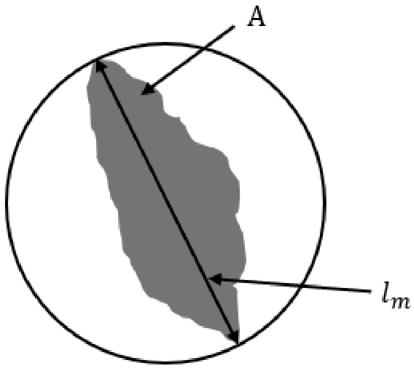

Figure 3.7*: Illustration of the Féret diameter of a graphite particle*

Using this method, several values were calculated to acquire information from the images. First, the nodularity was determined, for which graphite particles with a Féret diameter less than 10 µm were excluded, as according to ISO 945-4 (2019b). A circle was fitted around each of the remaining particles based on the Féret diameter, as illustrated in Figure 3.7. The roundness of these particles is required to calculate the nodularity and is defined as:

$$\rho = \frac{4 * A}{\pi * l_m^2}$$

Where ρ is the roundness, A is the area of the graphite particle, and l_m is the Féret diameter.

Based on the roundness, the nodularity was then calculated using (International Organization for Standardization, 2019b):

$$p_{nod} = \frac{A_{VI} + A_V}{A_{all}}$$

In this formula, p_{nod} is the nodularity, A_{VI} and A_V represents the total area of graphite particles with a roundness between 0.6 and 1.0, and A_{all} is the total area of all qualified graphite particles, regardless of their roundness.

Thereafter, the particle density was also calculated and expressed in particles/mm^2. The percentage of approved graphite particles was also determined using the total number of particles and the number of particles fulfilling the roundness criterion, calculated as:

$$Percentage\ of\ approved\ graphite\ particles = \frac{Number\ of\ particles\ fulfilling\ the\ roundness\ criterion}{Total\ number\ of\ particles}$$

Furthermore, each qualified graphite particle (with a Féret diameter of 10 µm or higher) was divided into a graphite shape to evaluate the most common shape in each sample. These groups were based on the roundness of the particle and expressed as area fraction of the total area. The roundness intervals for each shape are presented in Table 3.2 and are based on Riposan et al. (2022). Representative graphite particles from the real samples for each shape are shown in Table 3.3.

***Table 3.2**: Categorization of graphite shape based on roundness*

Graphite Shape	**Roundness, ρ**
I	$0 \leq \rho < 0{,}1$
III	$0{,}1 \leq \rho < 0{,}45$
IV	$0{,}45 \leq \rho < 0{,}6$
V	$0{,}6 \leq \rho < 0{,}8$
VI	$0{,}8 \leq \rho \leq 1$

***Table 3.3**: Representative graphite particles corresponding to each shape*

Shape I	**Shape III**	**Shape IV**	**Shape V**	**Shape VI**
				

For each sample, the distribution of graphite particle sizes was examined based on the Féret diameter and expressed as a fraction of the total area. All Féret diameter intervals and its representative size are shown in Table 3.4, based on (International Organization for Standardization, 2019a).

***Table 3.4**: Categorization of graphite size based on Féret diameter*

Graphite Size	**Féret diameter, l_m [µm]**
1	$1\,000 \leq l_m$
2	$500 \leq l_m < 1\,000$
3	$250 \leq l_m < 500$
4	$120 \leq l_m < 250$
5	$60 \leq l_m < 120$
6	$30 \leq l_m < 60$
7	$15 \leq l_m < 30$
8	$10 \leq l_m < 15$

3.2.4 Sample Etching

Etching was performed to reveal the microstructure and to determine whether any pearlite was present or if the material consisted solely of ferrite. The samples used for the etching process were samples P1, P2, and P6 on the parting line. Sample P5, from the middle section was also included. A 2% Nital solution, which consisted of 2% nitric acid and 98% ethanol, was used as the etchant. The sample surfaces were then immersed one by one in the solution, with each sample being etched for approximately 60 seconds. After the etching period, ethanol was immediately applied in a generous amount to stop the etching reaction. A heat gun was then used to dry the samples. Thereafter, the samples were left for approximately one hour, since newly etched samples may negatively affect the microscope lens. An optical microscope (Zeiss Axioscope 7) was used to investigate the microstructure with a magnification of 5X to scan the surface for different phases. Subsequently, images were captured at 10X magnification to document the microstructure. Additionally, SEM images of sample P5 were acquired using secondary electrons with a LEO 1550.

3.2.5 Hardness Testing

Before hardness testing, the same samples as mentioned in chapter 3.2.4, were ground and polished according to step 2 to 4 in Table 3.1 to obtain a surface unaffected by the etching. The hardness tests were performed using a Struers DuraScan-70 G5, testing the samples one at a time. A measurement pattern, illustrated in Figure 3.8 was created to ensure a representative evaluation of the hardness distribution within the samples. Three rows were positioned along the radial direction of each sample, with a spacing of 5 mm between the rows. In each row, 17 measurement points were selected with a spacing of 1 mm. The points closest to the edge were located approximately 1-2 mm from the edge of the sample. With indents approximately the size of 210 µm, the minimum distance between points exceeded the requirements of three times the indent size presented in the standard. For the edge, the standard distance should be 2.5 times the indent size which was significantly higher in these tests (International Organization for Standardization, 2023).

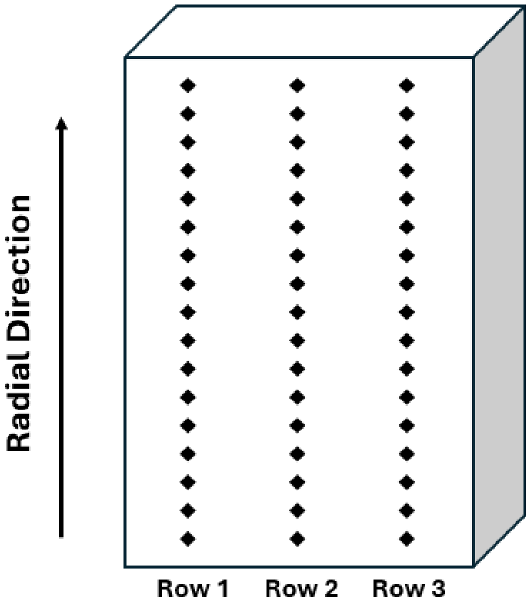

***Figure 3.8**: Illustration of the hardness indent distribution, 51 indents in total per sample*

The tests were performed using a Vickers (square-based pyramid) indenter with a load of 5 kgf (HV5) and a magnification of 20X for the images. During testing, the indenter was lowered onto the sample surface with the specified load applied for approximately 10 seconds before unloading and moving to the next measurement point automatically. After completion of all indentations, images of each indentation were captured. These images were subsequently used to determine the diagonals of each indentation mark, from which the Vickers hardness value (HV5) was calculated for every point. The HV5 values were then plotted and analyzed using a Python script.

3.3 Metal Cutting

This chapter describes the conducted material cutting. It begins with the cutting tests that were performed, including force measurements. Subsequently, wear on the cutting tools was examined using a stereo microscope. A Python script was developed to extract the cutting force data from the cutting tests. As a final step, SEM images of the tools were analyzed.

3.3.1 Cutting Tests

Cutting tests were performed on one pipe from wheel hub B and one from wheel hub C. Each pipe was machined from both ends, resulting in four sections in total. These sections were named LowerB and UpperB for wheel hub B, and LowerC and UpperC for wheel hub C (Figure 3.9). Before machining, both pipes were measured to ensure that the two upper parts and the two lower parts were at the exact same position in both pipes. Prior to the cutting tests, each part was turned internally and externally, to ensure identical geometry. Due to the draft angle used to facilitate mold removal during casting, the lower part had larger outer and inner diameters. Therefore, a safety margin was applied during measurement to guarantee the same SCL of 817.5 m for all parts, calculated using following formula:

$$SCL = \frac{D_{out}^2 - D_{in}^2}{4 * f} * \frac{\pi}{1000} * \frac{l}{a_p}$$

The formula includes the outer and inner diameter of the pipe (D_{out} & D_{in}), feed rate (f), cutting depth (a_p) and overhang (*l*).

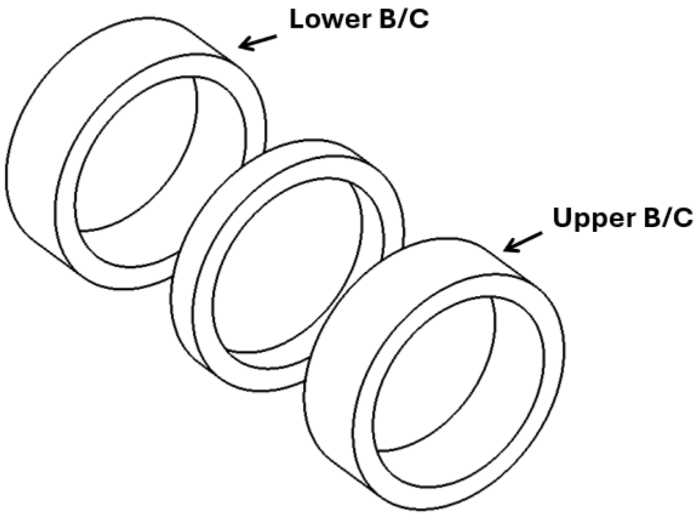

Figure 3.9*: Illustration of lower B/C and upper B/C for cutting tests*

To mount the workpiece as centered as possible, it was placed with its upper side against the chuck and clamped internally for stabilization. An EMCO Turn 365 CNC lathe, equipped with a dynamometer for cutting force measurement, was used to conduct the tests, as presented in Figure 3.10. The tools used were Sandvik Coromant CNMG120412-KRR3210 inserts, featuring an inscribed circle of approximately 12.7 mm, a thickness of around 4.8 mm and a nose radius of 1.2 mm. It consisted of cemented carbide as the substrate, with a multilayer chemical vapor deposition (CVD) coating: aluminum oxide (Al_2O_3) on top, titanium carbonitride (TiCN) beneath, and a thin titanium nitride (TiN) wear-indicating layer on the flank. All tests were performed as face turning operations. Each half of the workpiece was machined in five cycles, with six passages per cycle, resulting in a total of 45 mm of the pipe length being machined per half. All the tests had constant cutting speed (V_c), feed (*f*) and depth of cut (a_p), see values in Table 3.5. These parameters were chosen based on similar tool-workpiece combinations, the tool suppliers recommendations and to ensure sufficiently large SCL to reach reasonable wear amounts.

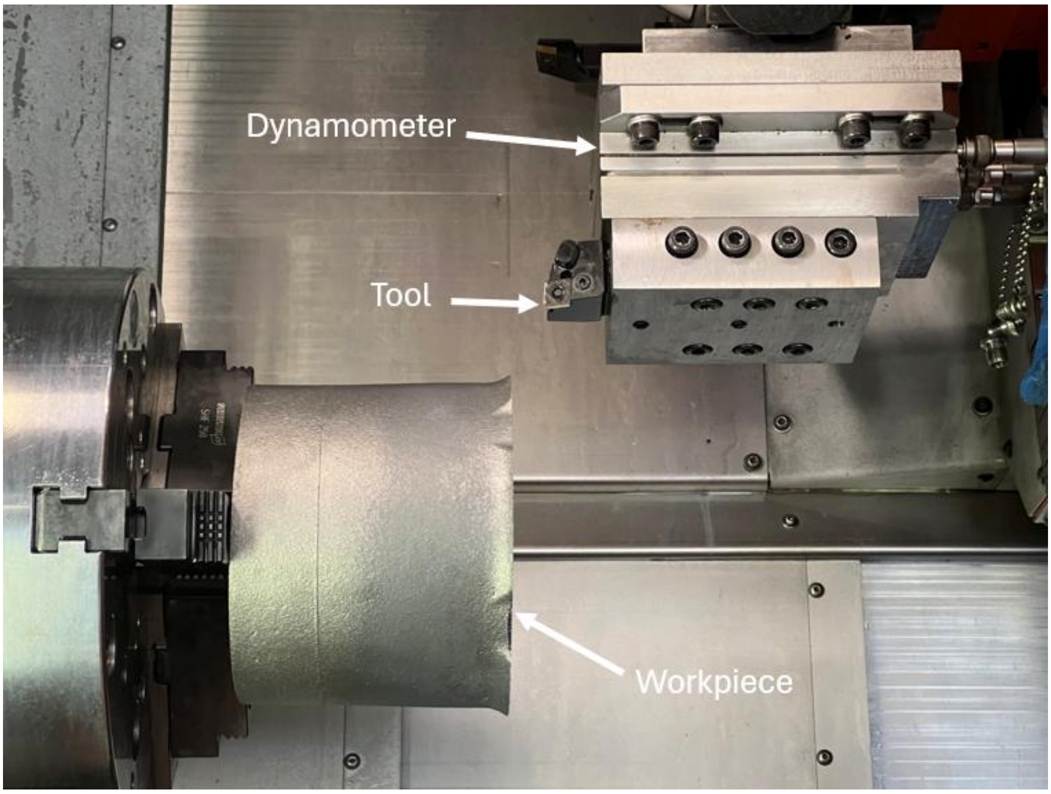

Figure 3.10: *The setup used for cutting tests*

Table 3.5: *Parameters used for the cutting tests*

Test \ Parameter	V_c [m/min]	f [mm/rev]	a_p [mm]	SCL [m]
1, 2, 3 & 4	275	0.2	1.5	817.5

3.3.2 Worn Tool Measurements

To measure the tool wear progression, a stereo microscope (SOM) (Zeiss Stereo Discovery V20) was used. The flank face of all tools was examined at 50X magnification. A Z-stacking feature of the microscope was used to obtain focus over a larger depth of field. Z-stacking stacks microscope images along the Z-axis together, and an algorithm generated a single image with the entire surface in focus. For each image, the maximum flank wear was measured. This procedure was performed after every cycle to monitor the progression of flank wear over time.

3.3.3 Python Script – Force Plotting

Another Python script was created to analyze the cutting forces from the turning operations. The script used a voltage file that had been converted into a text file for processing. A calibration factor was then applied to convert the voltage values into force values (N). Subsequently, all three forces, including cutting force (F_c), feed force (F_f) and passive force (F_p), were plotted as a function of time.

When the graph was plotted, none of the three forces were perfectly aligned with the zero-force line. Instead, a variation of approximately ± 6 N was observed between them, which indicated an incorrect zero offset. The measured force should had been 0 N when no machining was performed. Therefore, a method was developed to adjust the calibration error by ensuring that all forces were connected to the zero-force line at both the start and the end of the measurement. Two points at the beginning of the process were selected to align all three forces with 0 N, by adjusting the signals in this region. Thereafter, two points were selected at the end of the graph, and a linear reference line was created between the zero-adjusted start and end points.

Subsequently, two additional points were selected on the graph to determine the force between them. The script generated the average value over the selected time interval for all three forces. For the result, the second passage of the first cycle was used, as the first passage showed lower forces due to minor calibration differences between the tools. In addition, the last passage of the final cycle was also included in the result.

3.3.4 SEM Imaging of Tools

SEM was used to further investigate the cutting tools. Prior to analysis, the tools were cleaned. This process involved applying acetone to the tools, followed by brushing to remove dirt. The tools were then placed in an ultrasonic cleaner for ten minutes. Finally, they were rinsed with ethanol.

The SEM model used was a LEO 1550, with an accelerating voltage of 15 kV. Backscattered electrons were used to identify the different materials in the cutting tool. One overview image of each tool, as well as one image of the flank of a selected tool, were captured to illustrate the overall tool condition and the flank wear. In addition, the chemical composition was analyzed using Energy-dispersive X-ray spectroscopy (EDS).

4. Results

The results section is divided into two parts: material characterization and metal cutting tests.

4.1 Material Characterization

Several properties of the graphite particles were analyzed, including nodularity, particle density and percentage of approved graphite particles. Furthermore, both the shape distribution and size distribution of the particles were examined. Results from the microstructural analysis and the hardness measurements of selected samples are also included.

4.1.1 Graphite Analysis

Values for nodularity, particle density and percentage of approved graphite particles for the pipe samples are shown in Table 4.1. A notable variation was observed between the samples along the parting line, samples P1, P2 and P6. Sample P1 exhibited the highest nodularity at 85.0%, followed by sample P2 at 75.9% and sample P6 at 66.5%. A substantial difference was also found in the particle density, where sample P1 contained 550.7 particles/mm^2, compared to 288.6 particles/mm^2 in sample P2 and 299.3 particles/mm^2 in sample P6. The percentage of approved particles was significantly higher in sample P1 (81.4%) compared to sample P2 (57.8%) and decreased further in sample P6 (36.4%). The graphite morphology of each sample is shown in Figure 4.1.

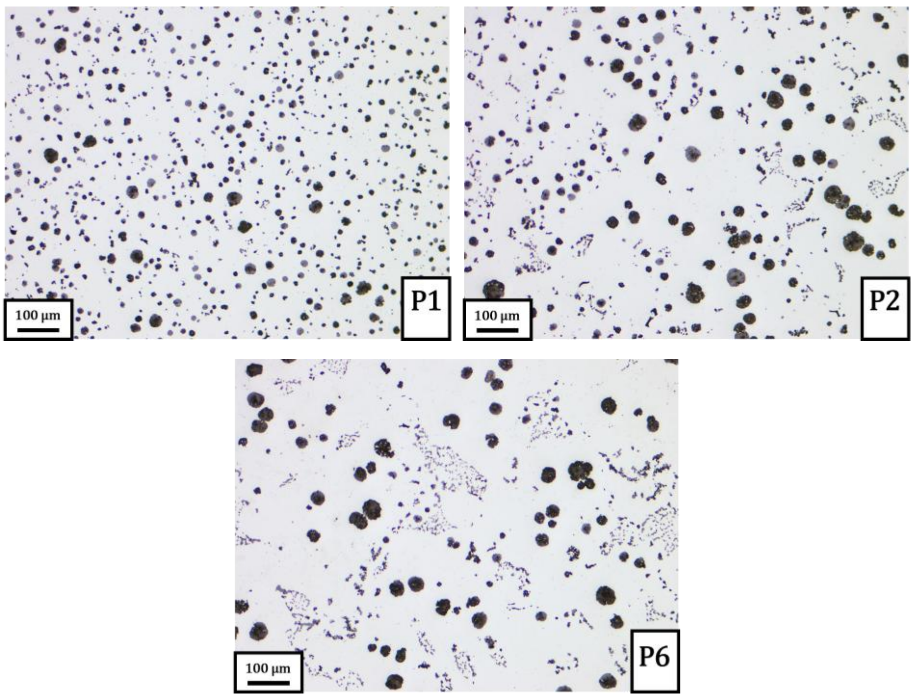

Figure 4.1: *Optical microscope images of the graphite morphology in samples P1, P2 and P6 respectively*

When comparing samples P2, P3, P4 and P5, within the same ring and pipe, samples P2, P3 and P4 showed similarities. These samples had a similar nodularity around 77% with a variation of about 1%. Furthermore, these samples exhibited closely matching particle densities of 288.6 particles/mm^2, 303.2 particles/mm^2 and 278.8 particles/mm^2, respectively. The percentage of approved particles was also similar, at 57.8%, 55.0% and 57.5%, respectively. In contrast, sample P5 showed significantly different values, with approximately 17 percentage points lower nodularity and a similar particle density to samples P2, P3, and P4. A difference was also observed in the percentage of approved particles, where sample P5 had approximately 13 percentage points lower. Closer examination of sample P5 revealed a variation in graphite morphology across the sample: the left side contained smaller and less rounded graphite particles, whereas the right side exhibited a morphology similar to the other samples in the ring. This variation is shown in Figure 4.2.

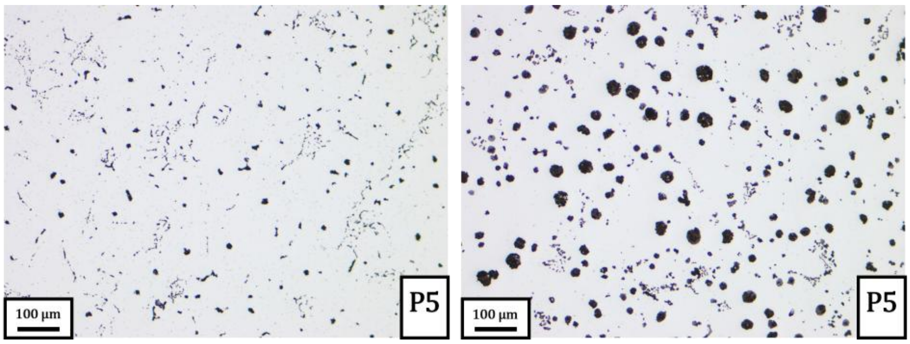

Figure 4.2: *Optical microscope images of the variation between left and right sides of sample P5*

Samples P7 and P8, located in wheel hubs B and C respectively, had similar values to samples P2, P3 and P4, positioned at the same vertical position. Although, sample P7 exhibited slightly lower nodularity and a lower percentage of approved particles.

Table 4.1: *Nodularity, particle density and percentage of approved graphite particles for the pipe samples*

Property / Sample	Nodularity	Particle Density [particles/mm^2]	Percentage of Approved Graphite Particles
P1	85.0%	550.7	81.4%
P2	75.9%	288.6	57.8%
P3	77.0%	303.2	55.0%
P4	77.0%	278.8	57.5%
P5	60.5%	307.6	44.1%
P6	66.5%	299.3	36.4%
P7	71.4%	299.7	51.7%
P8	75.3%	290.4	54.0%

Comparing the flange samples, the specific values for each sample are presented in Table 4.2. Only minor differences in nodularity were observed. Sample F2 exhibited the highest nodularity (82.8%), followed by sample F1 (78.1%), sample F4 (77.1%), and sample F3 (73.8%). Additionally, sample F2 had the highest particle density, with 506.8 particles/mm^2. The other samples showed similar values, with around 415 particles/mm^2 each. The percentage of approved graphite particles was also highest for sample F2 at 77.2%. Sample F4 had a percentage of 65.7%, followed by sample F1 at 63.1% and sample F3 at 59.5%.

***Table 4.2**: Nodularity, particle density and percentage of approved graphite particles for the flange samples*

Property / Sample	Nodularity	Particle Density [particles/mm^2]	Percentage of Approved Graphite Particles
F1	78.1%	406.0	63.1%
F2	82.8%	506.8	77.2%
F3	73.8%	431.8	59.5%
F4	77.1%	410.5	65.7%

4.1.2 Shape Distribution

The shape distribution of graphite particles for all pipe samples is provided in Table 4.3. Comparing samples P1, P2 and P6 from the parting line, sample P1 clearly exhibited the highest area fraction of highly rounded graphite particles (shape VI). Approximately 54.6% of the particles were shape VI, with sample P2 in second at 44.4%, while sample P6 showed a significantly lower value of 35.7%. Differences were also observed in the area percentage of less rounded particles (shape III). Sample P1 had the lowest proportion (5.7%), whereas sample P2 had higher percentage (12,3%) and sample P6 exhibited the highest value (19.6%).

Comparison of samples P2, P3, P4 and P5, located on the same ring, showed trends similar to those presented in chapter 4.1.1. Samples P2, P3 and P4 displayed similar shape distributions, with approximately 12% shape III particles and around 41% shape VI particles. In comparison, sample P5 had 22.9% shape III particles and a significantly lower area percentage of shape VI particles, at approximately 22.6%.

Furthermore, samples P7 and P8, from wheel hubs B and C respectively, showed values similar to samples P2, P3 and P4, placed at the same vertical position in the pipe. Minor tendencies were observed in sample P7, as it contained fewer highly rounded shaped (shape VI) than the others and a higher proportion of intermediate shapes.

Table 4.3: *Shape distribution of graphite particles for the pipe samples, expressed as area fraction of the total area*

Shape / Sample	I	III	IV	V	VI
P1	0.0%	5.7%	9.3%	30.4%	54.6%
P2	0.0%	12.3%	11.8%	31.5%	44.4%
P3	0.0%	12.3%	10.8%	38.5%	38.4%
P4	0.0%	10.9%	12.0%	33.9%	43.1%
P5	0.0%	22.9%	16.6%	37.9%	22.6%
P6	0.0%	19.6%	14.0%	30.7%	35.7%
P7	0.0%	12.5%	16.1%	36.2%	35.2%
P8	0.0%	12.0%	12.6%	32.5%	42.9%

Flange sample values of the shape distribution are summarized in Table 4.4. The observed trends indicated that sample F2 contained more rounded shaped graphite particles, with 48.7% classified as shape VI, compared with approximately 40% for the other samples. Samples F1, F3 and F4 showed larger area fractions of shape III and IV than sample F2.

Table 4.4: *Shape distribution of graphite particles for the flange samples, expressed as area fraction of the total area*

Shape / Sample	I	III	IV	V	VI
F1	0.0%	10.4%	11.5%	38.7%	38.4%
F2	0.0%	7.7%	9.5%	34.0%	48.7%
F3	0.0%	13.4%	12.8%	33.7%	40.1%
F4	0.0%	10.7%	12.2%	35.7%	41.4%

4.1.3 Size Distribution

Size classification results for graphite particles in all pipe samples are presented in Table 4.5. A comparison of samples P1, P2 and P6, positioned along the parting line, showed that sample P1 had the smallest graphite particles with respect to Féret diameter, containing only 0.1% in size 5 and 13.4% in size 6. In contrast, sample P2 exhibited 3.9% and 59.6% for the corresponding size classes. Furthermore, sample P6 showed an even larger difference, with 11.8% and 51.5% in size 5 and 6. The results also indicated that sample P1 had twice the percentage of size 7 compared with both sample P2 and P6, and approximately more than four to five times higher fraction of size 8.

Results for samples P2, P3, P4 and P5, situated in the same ring, revealed that the main difference was that sample P5 had a higher percentage of size 7 (46.3%) and a lower percentage of size 6 (42.3%), as compared with the other samples, which had around 59% and 31% respectively. The area fractions of size 5 and size 8 were similar across all samples.

Similar trends, as in chapter 4.1.1 and 4.1.2, was observed when comparing samples P7 and P8 to samples P2, P3 and P4, located at the same vertical position. Sample P8 was generally consistent with the other samples, although it showed slightly smaller graphite particles. More pronounced differences were observed in sample P7, which exhibited a higher area fraction of small particles compared to the other samples.

Table 4.5: *Size distribution of graphite particles for the pipe samples, expressed as area fraction of the total area*

Size / Sample	1	2	3	4	5	6	7	8
P1	0.0%	0.0%	0.0%	0.0%	0.1%	13.4%	64.6%	21.9%
P2	0.0%	0.0%	0.0%	0.5%	3.9%	59.6%	31.2%	5.0%
P3	0.0%	0.0%	0.0%	0.0%	5.6%	58.0%	31.1%	5.3%
P4	0.0%	0.0%	0.0%	0.0%	4.0%	59.6%	31.6%	4.8%
P5	0.0%	0.0%	0.0%	0.0%	3.1%	42.3%	46.3%	8.3%
P6	0.0%	0.0%	0.0%	0.0%	11.8%	51.5%	29.4%	7.3%
P7	0.0%	0.0%	0.0%	0.0%	5.0%	50.4%	37.5%	7.1%
P8	0.0%	0.0%	0.0%	0.0%	3.1%	54.8%	36.4%	5.7%

An overview of the size distribution for the flange samples is given in Table 4.6. The same trend observed previously persists, with sample F2 as the main outlier. It exhibited the highest percentage of size 8 (16.5%), which was nearly twice as high compared to the other samples. Furthermore, samples F2 and F3 showed similar values of approximately 60% of size 7, whereas samples F1 and F4 exhibited values around 10 percentage points lower. Sample F2 showed the lowest percentage of size 6 (22.2%), followed by sample F3 (31.0%), sample F4 (38.2%) and finally sample F1 (40.3%).

Table 4.6: *Size distribution of graphite particles for the flange samples, expressed as area fraction of the total area*

Size / Sample	1	2	3	4	5	6	7	8
F1	0.0%	0.0%	0.0%	0.0%	1.2%	40.3%	50.2%	8.4%
F2	0.0%	0.0%	0.0%	0.0%	0.4%	22.2%	60.9%	16.5%
F3	0.0%	0.0%	0.0%	0.0%	1.5%	31.0%	58.8%	8.7%
F4	0.0%	0.0%	0.0%	0.0%	4.5%	38.2%	47.2%	10.1%

4.1.4 Microstructure

For pipe samples P1, P2, P5 and P6, the microstructure was examined. P1, P2 and P6 were positioned along the same parting line, while P5 was located on the same ring as P2. Figure 4.3 shows a representative image from each sample, where the white grains are ferrite. For samples P1, P2 and P6, it was observed that the microstructure contained extremely little pearlite (less than approximately 1%). Instead, the microstructure consisted almost entirely of ferrite. This is also applicable on the right side of sample P5.

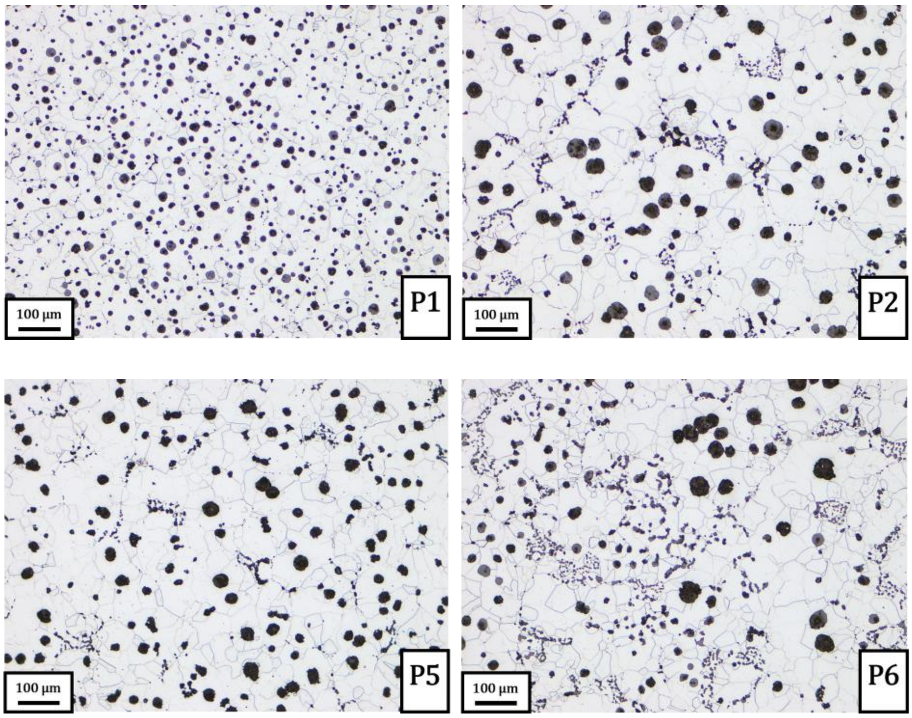

Figure 4.3*: Optical microscope images of etched samples P1, P2, P5 and P6 respectively*

The main difference was discovered in the protruding region of sample P5, earlier referred to as the left side, which appeared notably different after etching, presented in Figure 4.4. This region was initially considered to potentially had contained pearlite, due to imaging showing similarities of pearlite structure and was therefore investigated further. A scanning electron microscope (SEM) using secondary electrons was employed to examine the microstructure in greater detail, as shown in Figure 4.5. The observations indicated that the differing region was not pearlite.

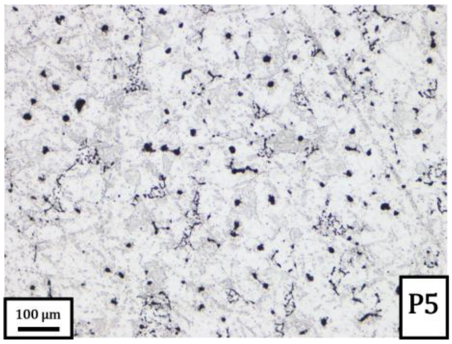

Figure 4.4: Optical microscope image of the left side of etched sample P5

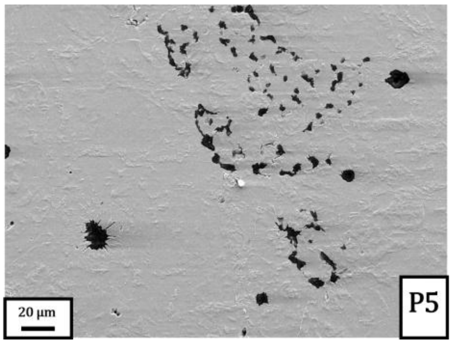

Figure 4.5: SEM image of the left side of etched sample P5, obtained at an accelerating voltage of 15 kV

4.1.5 Hardness Tests

Hardness tests were performed on the same pipe samples that were etched, P1, P2, P5 and P6. The test used HV5 and the values obtained for each row, see Figure 3.8, together with the average values, are provided in Table 4.7. Samples P1 and P2 had similar average HV5 values. Where sample P1 had remarkably low variation between the rows, with a deviation of ± 0.06 HV5. Sample P5 had the second lowest average hardness value at 197.0 HV5, followed by sample P6, which had the lowest average at 194.5 HV5.

***Table 4.7**: Hardness values for each row of each sample, including average values*

Row / Sample	Row 1 [HV5]	Row 2 [HV5]	Row 3 [HV5]	Average [HV5]
P1	199.5	199.4	199.5	199.5
P2	196.9	200.9	199.8	199.2
P5	197.3	195.9	197.7	197.0
P6	193.8	193.9	195.7	194.5

4.2 Metal Cutting Tests

In this chapter, the changes in flank wear for the different pipes are presented. Furthermore, the cutting forces recorded during the cutting tests are reported. The results from the SEM images of the cutting tools are also shown.

4.2.1 Flank Wear

The maximum observed flank wear for all tested pipes is presented in Figure 4.6. A cutting speed of 275 m/min was used for all tests, and the total SCL per half was 817.5 m. An overall trend was the small differences in maximum flank wear between the two lower pipes in each cycle, with an average difference of 2.8 µm. In contrast, the two upper pipes showed a larger average difference of 17.3 µm per cycle. After cycle five, the upper pipe from wheel hub B reached a maximum flank wear of 174.4 µm, which was 13.7 µm lower than the upper pipe from wheel hub C. The lower pipe from wheel hub B reached 155.7 µm, while the lower pipe from wheel hub C was deviating 1.8 µm. Comparing the average maximum flank wear after cycle five, the upper and lower pipes, combined separately, revealed a significant difference of 26.5 µm.

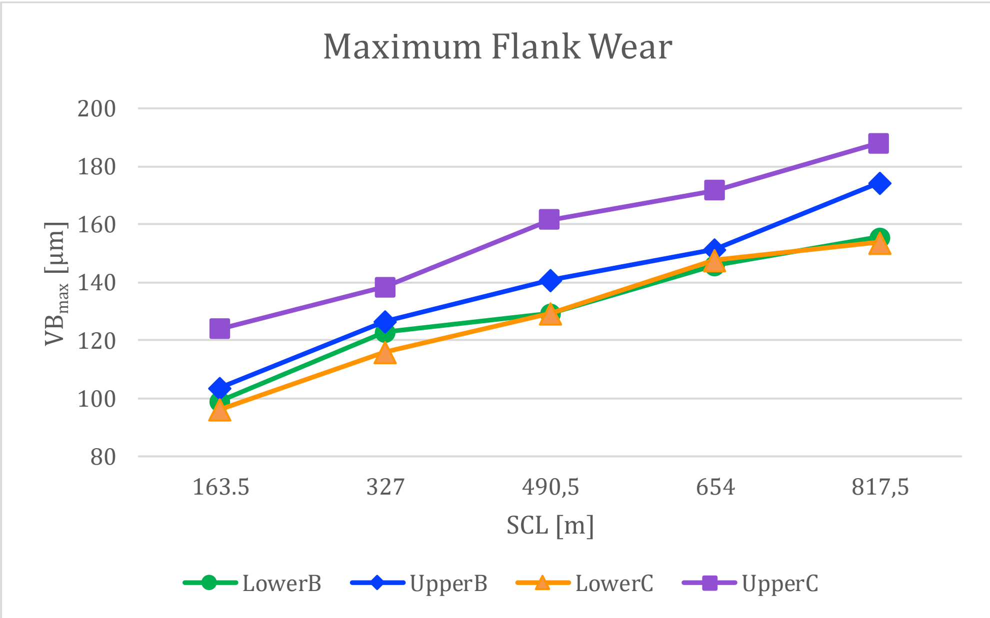

Figure 4.6*: The change in flank wear during the cutting tests for the four pipes*

4.2.2 Cutting Forces

The changes in cutting forces during turning as the tools progressed from a new to a worn condition are shown in Figure 4.7. In this context, the term "worn" refers to the tool condition after cycle five had been performed. The upper pipe of wheel hub C showed the highest force values in the worn tool condition compared with the other pipes, with a cutting force of 633.6 N, a feed force of 448.7 N and a passive force of 320.0 N. This correlates with the highest maximum flank wear. Furthermore, the worn state forces of the upper pipe of wheel hub B were more similar to those of the lower pipes rather than its equivalent upper pipe. It is notable that this pipe had the second highest maximum flank wear, approximately 12.7% higher than the two lower pipes. The final passage in cycle five was used for comparison, as it was considered most relevant when relating the forces to flank wear, even though the largest forces were recorded in the first passage.

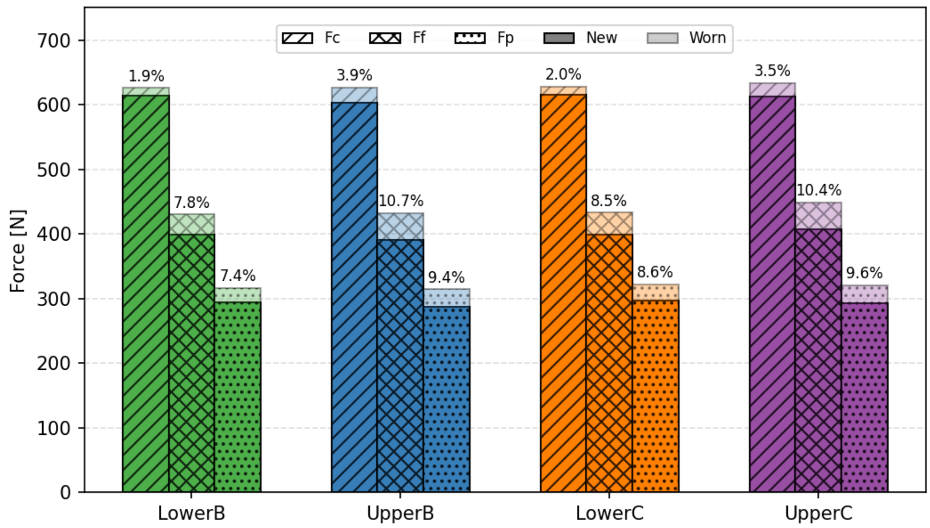

***Figure 4.7**: F_c, F_f & F_p for first passage in a test (new) and last passage in a test (worn), including the percentage increase*

To compare the tool forces, the resultant of the three forces (F_c, F_f and F_n) was calculated. The results, together with the percentage increase, are shown in Table 4.8. Both lower pipes had a similar percentage increase, and the same trend was observed for the two upper pipes. The main difference was the initial lower resultant force of the upper pipe from wheel hub B compared with the others. For the worn tool condition, the largest resultant force was observed for the upper pipe from wheel hub C (839.7 N), followed by the lower pipe from wheel hub C (827.8 N), the upper pipe from wheel hub B (823.4 N) and lastly the lower pipe from wheel hub B (822.7 N).

***Table 4.8**: Resultant force for the four pipes with new and worn tools, including percentage increase from new to worn state*

State / Pipe	New [N]	Worn [N]	Increase
LowerB	789.2	822.7	4.2%
UpperB	773.7	823.4	6.4%
LowerC	791.1	827.8	4.6%
UpperC	790.8	839.7	6.2%

4.2.3 SEM Images

A SEM image of the flank face was taken. Figure 4.8 shows the flank of the cutting tool used for the upper pipe of wheel hub C, including the positions of the coating layers; titanium carbonitride (TiCN), aluminum oxide (Al_2O_3), and titanium nitride (TiN), as well as iron-rich adhesion (Fe). The chemical composition of coating layers and adhered material was confirmed using Energy-dispersive X-ray spectroscopy (EDS). The figure also illustrates how the flank wear was determined. The maximum flank wear was measured from the top of the tool down to where the darker aluminum oxide layer ends, which is illustrated by VB_{max}.

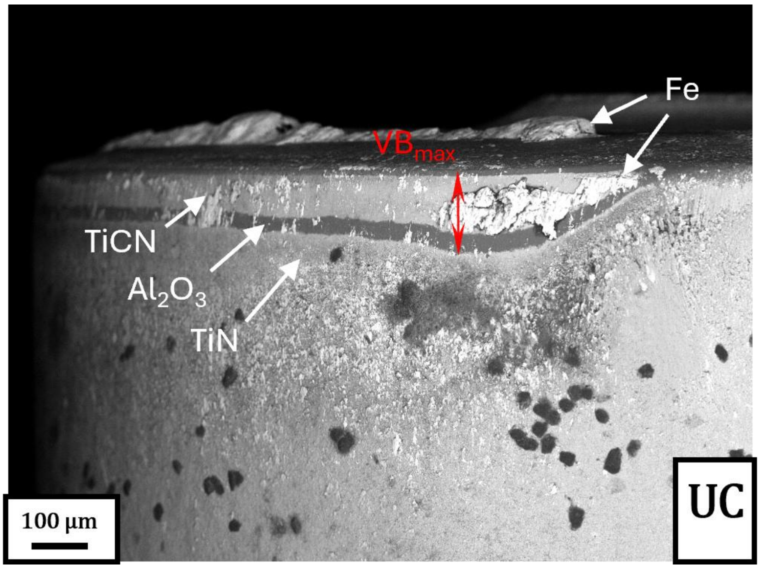

Figure 4.8*: SEM image showing the flank of the tool used for UpperC, illustrating coatings position, iron-rich adhesion, and the maximum flank wear, obtained at an accelerating voltage of 15 kV*

SEM overview images were captured for each cutting tool, as shown in Figure 4.9. The images indicate that the tools were not worn down to the cemented carbide. Instead, wear was observed within the coating layers, particularly the titanium carbonitride layer, which appears as the lighter region, while the surrounding darker region corresponds to aluminum oxide. In addition, significant iron-rich adhesion was observed on the rake and flank face. All cutting tools had similar overall wear and adhered material, with only minor differences between them.

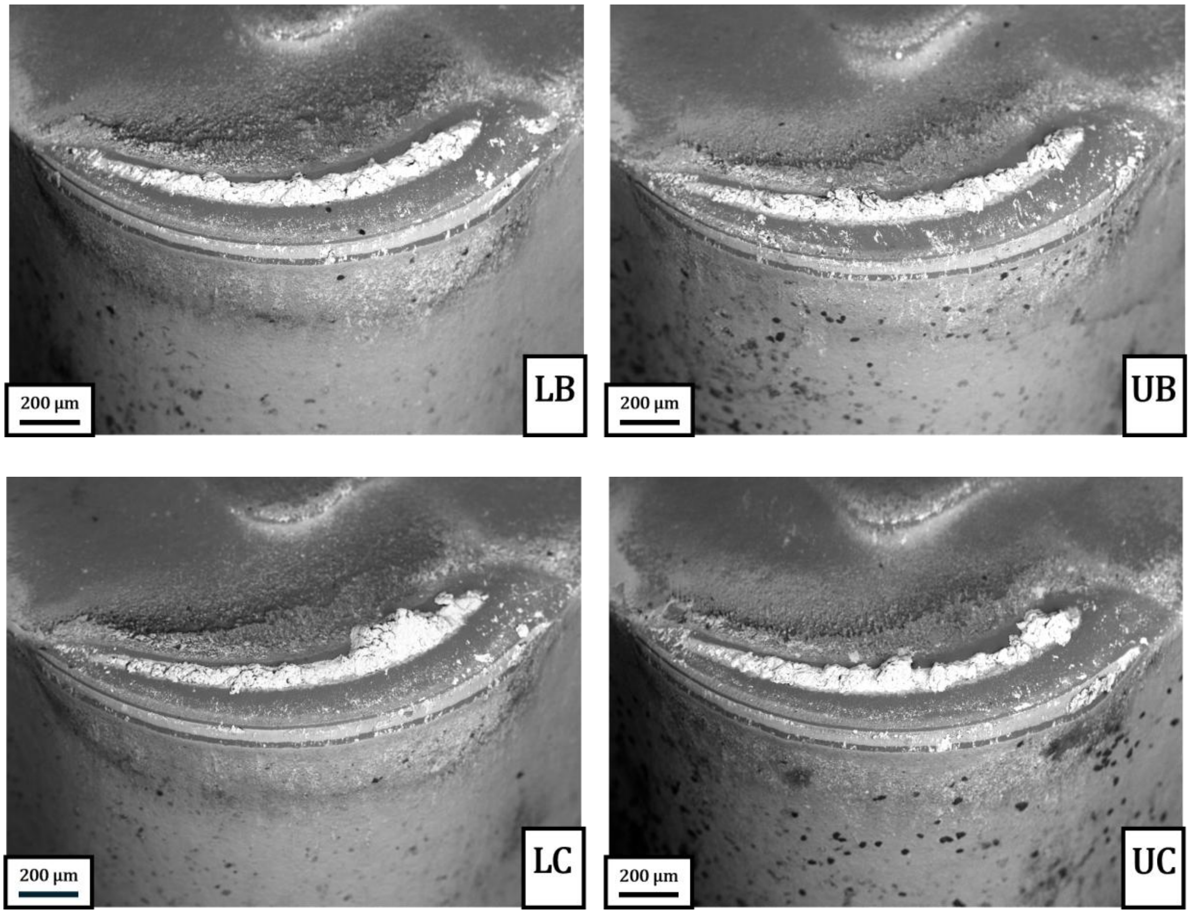

Figure 4.9*: SEM images showing an overview of the tools used for LowerB, UpperB, LowerC and UpperC, obtained at an accelerating voltage of 15 kV*

5. Discussion

This section is a discussion of the results mentioned in chapter 4. The chapter starts with a discussion of material characterization, specifically graphite particles, microstructure, and hardness testing. Metal cutting tests are also discussed with flank wear and cutting forces, as well as SEM images of the cutting tools.

5.1 Variations in Material Characteristics

The samples along the parting line have a decreasing percentage of nodularity moving from sample P1, through samples P2 and P6 in wheel hub A. Sample P1 was located at the upper section of the pipe, and the higher nodularity could be explained by faster cooling in the casting process as argued by Di Egidio et al. (2025). It is substantially different from sample P6, located at the lower part of the pipe, where cooling rate during casting would be slower due to its central location of the hub. The same theory can also be applied to the percentage of approved particles, where the amount decreases as we move from the upper part of the pipe towards the lower part. As Di Egidio et al. (2025) states, the cooling rate could also explain the major differences in particle density between sample P1 and the other samples, as both sample P2 and P6 were located closer to the center of the hub. However, it deviates from the nodularity and number of approved particles where the differences are apparent between each sample. For further confirmation of these trends, more samples in the different sections along P1 and P6 as performed for the middle section with P2 are needed. This also applies for samples on more hubs.

Sample P2, P3, P4 and P5 were all placed within the same distance from the upper section of the pipe in a ring. Using the same theory, that cooling rate is the main cause for the variations, the values from sample P2 would correlate with the remaining samples of the ring. While sample P2, P3 and P4 all share similar values of nodularity, particle density and percentage of approved particles, the values of sample P5 deviate. These differences could, however, be due to local variations as shown in the deviation of graphite morphology across P5 (Figure 4.2). This could be due to differences in cooling rate in the casting process. Di Egidio et al. (2025) argues that there is a strong correlation between solidification rate and the microstructure. Alternatively, Buschow et al. (2001) explains that the amount of magnesium is important when alloying nodular cast iron, where an incorrect amount could lead to variations in graphite shapes. This suggests that differences in magnesium content may have contributed to the observed differences in the material. Finally, the values of sample P7 and P8, with corresponding position of samples P2 to P5 in wheel hub B respectively C, also correlate with samples P2 to P4, with a small deviation for sample P7.

The argument that samples with a faster cooling rate are generating higher values of nodularity are also applicable when analyzing the flange samples. As the flange is an outer part of the hub, the cooling rate would be faster in this area. Sample F2, located at edge of the hub and the flange, had the highest percentage of nodularity with values similar to sample P1. The high nodularity of sample F1, at the thinnest part of the flange, strengthens the argument further.

When analyzing the results of shape distribution, it is noticeable that it follows the trends mentioned of nodularity and particle density. Sample P1 had the highest percentage of shape VI and the lowest amount of shape III, meaning that the roundness improves closer with faster cooling, as described by Di Egidio et al. (2025). The same analysis can be drawn with the flange samples where sample F2 had a similar distribution. Moving towards the center of the hub leads to decreased area fraction of shape VI while increased area fraction of shape III, resulting in more flake shaped graphite particles.

Size distribution strengthens the argument further. The result showed a significantly higher percentage of smaller graphite particles for sample P1 compared to the other pipe samples, with sample F2 also containing smaller particles. Slower cooling in central parts of the hub increases the sizes of graphite particles, which could be an effect of the particles having more time to merge. Di Egidio et al. (2025) also argues that the nodule size increases with longer solidification time. This correlates with sample P6 having significantly higher area fraction of size 5. The merging could also explain the shift in shape distribution for samples P2 to P8.

When analyzing the microstructures of samples P1, P2, P5 and P6 from wheel hub A, they consisted mainly of ferrite. Some concerns were initially raised regarding sample P5, as its appearance differed from the other samples. However, this was confirmed to be ferrite by the SEM analysis. Since all samples primarily exhibited ferrite, it is reasonable to conclude that the overall microstructure of the pipe was ferrite. It is also important to note that all samples were repolished after etching prior to the hardness tests. Sample P5 was then re-examined after polishing and subsequently exhibited graphite values similar to those of samples P2, P3 and P4 located on the same middle ring of wheel hub A. This suggests that the initial deviation was likely to be a local defect from the casting process, resulting in over-etching on the deviating side. Another explanation is issues during grinding and polishing, where sample P5 might not have been properly mounted, resulting in an uneven polishing angle and consequently incomplete polishing of certain areas. It could also have been due to polishing suspension smeared into that region, causing it to act differently.

The same samples used for etching were subsequently used in the hardness tests. When comparing samples P1 and P6, which were located on opposite sides of the pipe, a notable difference in hardness was observed between them, 199.5 HV5 compared to 194.5 HV5, respectively. This variation may be related to the nodularity and the percentage of approved graphite particles. Although sample P2 exhibited a hardness value similar to sample P1, it is justified to assume that nodularity has some influence on the hardness of the material, which is also stated by Di Egidio et al. (2025). The difference between samples P2 and P5, located on the same ring, was on average 2.2 HV5, which may be due to local variations in the material.

If a linear relationship between the hardness and nodularity existed, sample P5 would better support this trend, as its hardness was better distributed between sample P1 and P6 compared to sample P2. Examining sample P2 in more detail, rows 2 and 3 showed higher hardness compared to row 1, with a difference of approximately 3.5 HV5. This difference may also be explained by local deviations, as Chikali and Shinde (2020) note that nodular cast iron produced industrially typically exhibits microstructural variations within a component.

5.2 Tool Wear and Cutting Forces

The maximum flank wear of the two lower pipes had values with similar progression, which could indicate that the material in these parts was similar. In contrast, the upper pipes showed a larger difference in maximum flank wear over time. The upper pipe from wheel hub C consistently exhibited higher flank wear compared to the upper pipe from wheel hub B. This may have been caused by local defects and material variations described by Chikali and Shinde (2020), which were also observed in sample P5. These local defects could potentially be due to differences in material composition as Buschow et al. (2001) suggests, affecting material performance. Another possible explanation is that cooling rate may have contributed to the observed results (Di Egidio et al., 2025).

When comparing the maximum flank wear between upper and lower pipes, it is evident that the upper pipes had higher flank wear overall. One possible explanation is that the hardness was higher at the top of the pipe and lower at the bottom, as shown in samples P1, P2, P5 and P6. According to a study made by Senthilkumar et al. (2014), increased hardness results in greater flank wear, which was consistent with the results obtained from the cutting tests. Another contributing factor may be the higher nodularity observed in the upper pipes, which has also been associated with increased flank wear (de Sousa et al., 2017).

The difference in flank wear between the upper pipes could also be related to the differences observed in sample P7 from wheel hub B and sample P8 from wheel hub C. Sample P7 exhibited lower nodularity and a lower percentage of approved graphite particles than sample P8. This could have influenced the flank wear, as de Sousa et al. (2017) reported that well-rounded graphite particles are more difficult to machine than flake shaped graphite particles due to stress concentrations associated with flake graphite during machining. However, the limited number of wheel hubs makes a general conclusion difficult. Instead, the differences presented can be used as a basis for further studies.

The increase in cutting forces followed a similar pattern in both upper pipes, corresponding with the flank wear results, as these pipes also exhibited the highest flank wear. The two lower pipes showed a smaller increase in cutting forces, however, the increase was similar between them, which corresponded to their nearly identical flank wear values. This is consistent with the findings of Acharya (2023), who reported that increased flank wear results in higher cutting forces. It is also important to note that steady state, commonly considered as five seconds of cutting, was not achieved during the cutting tests, as each machining passage lasted approximately four seconds. This introduces some uncertainty in the measurements.

Furthermore, differences could also be observed in resultant force in worn state. The highest resultant force was measured for the upper pipe in wheel hub C, which corresponds to it exhibiting the highest maximum flank wear. This may be explained by the higher nodularity and hardness in this pipe (de Sousa et al., 2017; Ren et al., 2019). On the other hand, the same pattern was not observed for the upper pipe in wheel hub B, as it had a resultant force similar to those of the lower pipes. This could have been caused by local deviations in the material.

SEM images showed that the tools were only worn down to the titanium carbonitride layer and not to the cemented carbide, indicating that a portion of the tool life remained. This implies that the cutting tests cannot be used for an end-of-life analysis. However, this provides good insight into the wear process, as the tools were in an intermediate stage of their tool life. The intermediate stage is advantageous for studies investigating wear mechanisms compared to fully worn tools, as they may be too damaged to be analyzed. Finally, a notable observation was the adhered iron on the rake face, suggesting that this nodular cast iron exhibits adhesive behavior during machining.

6. Conclusion & Recommendations

This degree project studied material characteristics and machinability of nodular cast iron comparable to EN-GJS-500-14. Three wheel hubs were received from Volvo, on which the graphite, microstructure and hardness were examined to investigate the material properties. To evaluate the machinability, cutting tests were performed and during this process tool wear and cutting forces were measured. In addition, SEM images were captured to analyze the cutting tools. From these tests, conclusions were drawn, as presented below:

- There were clear differences in the graphite morphology within components depending on the position in the wheel hub. The results show that outer sections of the wheel hub resulted in increased nodularity and smaller graphite particles, whereas the inner sections presented a lower nodularity and larger graphite particles. Indicating that cooling rates might be of great significance.
- Comparing corresponding samples from different hubs with the results from within one hub, the differences in graphite properties are minor. Further research is required to draw any conclusions.
- The material consisted primarily of ferrite, and the hardness in the pipe corresponded to the position in the hub, with outer sections leading to increased hardness. The hardness correlates with the graphite properties to some extent.
- A correlation was found between maximum flank wear and resultant force for the upper and lower section, where an increased maximum flank wear resulted in a higher resultant force.
- The upper sections, with increased nodularity and hardness, had a higher maximum flank wear compared to the sections with lower parameters. However, the cutting forces can only explain these correlations to some extent, since one upper section had a similar resultant force in worn tool state to both lower sections. Further investigation is required to see whether graphite properties or hardness has the most influence.

Recommendations for further development of the work performed in this degree project are presented below:

- Focus more on the casting process of the wheel hubs. This includes following the process from casting to testing to identify potential deviations in the casting that could explain variations in the material. Furthermore, casting simulation could be a tool to detect possible irregularities and determine the differing cooling rates in the cast.

- Additional testing is recommended to achieve stronger statistical basis, especially for the turning operations, as more pipes need to be machined. The conclusion drawn from the four machine test limits statistical reliability.
- Another recommendation is to perform the same sample tests, conducted for wheel hub A, on additional wheel hubs to confirm the observed differences shown between the samples.
- Material characterization includes a lot of properties that can be studied. Further research should include more of these to broaden the knowledge on the material. For example, investigating the non-metallic inclusions in the material.

References

Acharya, D. (2023). *The impact of tool wear on CNC machining defects*. ProleanTech. https://proleantech.com/the-impact-of-tool-wear-on-cnc-machining-defects/

Andersson, D. & Aronsson, M. (2024). *Machinability of 100Cr6 bearing steels* [Master thesis, Chalmers University]. Chalmers student theses. https://hdl.handle.net/20.500.12380/308683

ASM International. (1988). *ASM handbook* (Vol. 15, *Casting*).

Astakhov, V. (2014). *Machinability: Existing and advanced concepts*. https://doi.org/10.1002/9781118576854.ch1

Buschow, K.H., Cahn, R., Flemings, M.C., Ilschner, B., Kramer, E.J., Mahajan, S. (2001). *Encyclopedia of materials - Science and technology, Volumes 1-11 - Cast Irons.* Elsevier. https://www.sciencedirect.com/referencework/9780080431529/encyclopedia-of-materials-science-and-technology

Chikali, P. B., & Shinde, V. D. (2020). *Analysis of machinability in ductile iron casting*. Materials Today: Proceedings, 27(1), 584-588. https://doi.org/10.1016/j.matpr.2019.12.064

Daicu, R., & Oancea, G. (2022). *Methodology for measuring the cutting inserts wear*. Symmetry, 14(3), 469. https://www.mdpi.com/2073-8994/14/3/469

Denkena, B., Krödel, A., & Ellersiek, L. (2021). *Influence of metal working fluid on chip formation and mechanical loads in orthogonal cutting*. The International Journal of Advanced Manufacturing Technology, 118, 3005–3013. https://doi.org/10.1007/s00170-021-08164-2

De Sousa, J.A.G., Sales, W.S & Machado, A.R. (2017). *A review on the machining of cast irons*. Int J Adv Manuf Technol, 2018, 94:4073-4092. https://.doi.org/10.1007/s00170-017-1140-1

Di Egidio, G., Ferro, P. & Morri, A. (2025). *Microstructure in non-standard heavy section ductile iron castings: influence of solidification time and casting size*. J. Iron Steel Res. Int. 32, 4249–4263 . https://doi.org/10.1007/s42243-025-01598-y

El-Hofy, H. A.-G. (2013). *Machinability. Fundamentals of machining processes (2nd ed.)*. CRC Press. https://doi.org/10.1201/b15339

ESMA. (n.d.). *Sintering – Cost-effective manufacturing of complex components*. https://esma.se/en/component-manufacturing/sintering/

Hiratsuka, S. (2022). *Microstructure and mechanical properties of cast iron* (KAYABA Technical Review No. 64). KYB Corporation. https://www.kyb.co.jp/english/technical_report/data/no64e/editorial.pdf

HN Carbide. (n.d.). *Why does tool life suddenly drop? A practical guide to cutting tool life, wear mechanisms, and smarter carbide tool selection*. https://hncarbide.eu/why-does-tool-life-suddenly-drop-a-practical-guide-to-cutting-tool-life-wear-mechanisms-and-smarter-carbide-tool-selection/

Huda, Z. (2025). *Metal casting engineering*. Springer Cham. https://doi.org/10.1007/978-3-031-84620-5

International Organization for Standardization. (2019a). *Microstructure of cast irons - Part 1: Graphite classification by visual analysis*. (ISO Standard No. 945-1:2019). https://www.iso.org/standard/77568.html

International Organization for Standardization. (2019b). *Microstructure of cast irons - Part 4: Test method for evaluating nodularity in spheroidal graphite cast irons*. (ISO Standard No. 945-4:2019). https://www.iso.org/standard/69360.html

International Organization for Standardization. (2023). *Metallic materials – Vickers hardness test – Part 1: Test method*. (ISO Standard No. 6507-1:2023). https://www.iso.org/standard/83898.html

ISCAR. (n.d.). *Get to know cutting tools: Machining calculations*. https://www.iscar.com/Catalogs/Publication/english_1/Cutting_tools_user_guide/Cutting_tools_user_guide.pdf

Kistler. (n.d.). *Cutting forces in turning operations*. https://www.kistler.com/SE/en/cutting-forces-in-turning-operations/C00000103

Klocke, F. (2011). *Manufacturing process 1*. RWTH Aachen University. DOI: 10.1007/978-3-642-11979-8

Luque, A., Aldazabal, J., Martínez-Esnaola, J. M., & Gil Sevillano, J. (2010). *A moelcular dynamics simulation of the strength of cementite Fe3C*. In Multiscale Materials Modeling: 5th International Conference, MMM 2010 (p. 469). Fraunhofer Institute for Mechanics of

Materials IWM.
https://www.iwm.fraunhofer.de/content/dam/iwm/en/Why%20IWM/Scientific_Excellence/Scientific_Publications/Fraunhofer_IWM_scientific_publications/MMMProceedings/MMM2010_4_Microstructure%20Modeling.pdf

Manek Casting. (2024). What is *iron casting?* https://manekcasting.com/iron-casting/

Meyers, A.R., Slattery, T.J. (2001). *Basic machining reference handbook (2nd Edition) - 3. Turning and the lathe: Definition and History.* Industrial Press.
https://app.knovel.com/hotlink/pdf/id:kt008VYMC4/basic-machining-reference/turning-lathe-definition

Modulus Metal. (n.d.). *EN GJN HV600, former BS 2C, mechanical properties, cast iron, white Ni-Cr alloy*. https://www.modulusmetal.com/en-gjn-hv600-former-bs-2c-mechanical-properties-cast-iron-white-ni-cr-alloy/

Mori, F., Ötting, M., & Tonn, B. (2025). *Objective description of graphite morphology in ductile cast iron by numerical geometric parameters. International Metalcast 20, 1922-1935*. Advance online publication. https://doi.org/10.1007/s40962-025-01706-4

Nanoscience Instruments. (n.d.). *Scanning electron microscopy*.
https://www.nanoscience.com/techniques/scanning-electron-microscopy/

Nayyar, V., Kaminski, J., Kinnander, A. A., & Nyborg, L. (2012). *Experimental investigation of machinability of graphitic cast iron grades; Flake, compacted and spheroidal graphite iron in continuous machining operations*. Procedia CIRP, 1(1): 488-493.
http://dx.doi.org/10.1016/j.procir.2012.04.087

Nuclear Power. (n.d.). *Ferrite*. https://www.nuclear-power.com/nuclear-engineering/materials-science/phase-diagrams-of-iron-carbon-system/ferrite/

Orłowicz, A.W., Mróz, M., Tupaj, M. & Trytek, A. (2015). *Materials used in the automotive industry*. Archives of Foundry Engineering. ISSN (1897-3310), Volume 15. Issue 2/2015 p.75-78. doi.10.1515/afe-2015-0042

Penticton Foundry. (2016). *ASTM A532 Class I Type A*.
https://www.pentictonfoundry.com/news/astm-a532-class-i-type-a/

Rao, C.J., Rao, D.N. & Srihari, P. (2013). *Influence of cutting parameters on cutting force and surface finish in turning operation*. Procedia Engineering,Volume 64, p. 1405-1415, ISSN 1877-7058. https://doi.org/10.1016/j.proeng.2013.09.222.

Ren, J., Li, Zl., Xiong, Y., Li, F., Ren, F., & Volinsky, A. A. (2019). *Effect of microstructure and mechanical properties on cutting force of different cast irons with similar tensile strength*. *China Foundry* 16, 177–183. https://doi.org/10.1007/s41230-019-8136-4

Riposan I, Anca D, Stan I, Chisamera M, Stan S. (2022). *Graphite nodularity evaluation in high-Si ductile cast irons*. Materials, 15(21), 7685. https://doi.org/10.3390/ma15217685

Rundman, K. B. (2001). *Cast irons* (including 15 Compacted Graphite Iron). In *Encyclopedia of materials: Science and technology*. Elsevier. https://doi.org/10.1016/B0-08-043152-6/00186-8

Sabner. (n.d.). *Järn-kol-fasdiagram*. https://sabner.com/sv/jarn-kol-fasdiagram/

Sandvik Coromant. (n.d.a). *Cutting tool materials*. https://www.sandvik.coromant.com/en-us/knowledge/materials/cutting-tool-materials

Sandvik Coromant. (n.d.b). *External turning*. https://www.sandvik.coromant.com/en-us/knowledge/general-turning/external-turning

Sandvik Coromant. (n.d.c). *How to improve tool life in turning*. https://www.sandvik.coromant.com/en-us/knowledge/general-turning/how-to-improve-tool-life-in-turning

Sandvik Coromant. (n.d.d). *Wear on cutting edges*. https://www.sandvik.coromant.com/en-us/knowledge/materials/wear-on-cutting-edges

Seco Tools. (n.d.). *Tool wear patterns in machining*. https://www.secotools.com/article/tool_wear_patterns_in_machining

Senthilkumar, N., Ganapathy, T., & Tamizharasan, T. (2014). *Optimisation of machining and geometrical parameters in turning process using Taguchi method*. *Australian Journal of Mechanical Engineering*, *12*(2), 233–246. https://doi.org/10.7158/M12-113.2014.12.2

Shenzhen Tuofa Technology. (2025). *Tool wear patterns explained: Common types, causes, and effective solutions*. https://www.tuofamachining.com/news/tool-wear-patterns-explained-common-types-causes-and-effective-solutions-276982.html

Sild, S. (2024). *Sand casting – Process, sand properties, pros & cons*. Fractory. https://fractory.com/sand-casting-explained/

Sing, R. (2016a). *Gray cast iron*. In *Applied welding engineering*. Elsevier. https://doi.org/10.1016/B978-0-12-804176-5.00007-4

Sing, R. (2016b). *White cast iron*. In *Applied welding engineering*. Elsevier. https://doi.org/10.1016/B978-0-12-804176-5.00007-4

TechMet. (2025). *Tool wear: Flank wear*. https://www.techmet-carbide.com/blog/131/tool-wear-flank-wear?srsltid=AfmBOorUYqukYbdN9Xw-4uHdnvkc-DARjC9AgiwT2-C3NochJdFrSWg9

Thermo Fisher Scientific. (n.d.). *Electrons in SEM*. https://www.thermofisher.com/se/en/home/materials-science/learning-center/applications/sem-electrons.html

Trent, E.M., Wright, P.K., Dearnley, P.A. (2025). *Metal cutting - Theory, selection, and design (5th Edition) - 2.3 Turning or turn-cutting.* Elsevier. https://app.knovel.com/hotlink/epub/rcid:kpMCTSD001/id:kt014CBLX1/target:s0020/metal-cutting-theory/turning-or-turn-cutting

U.S. General Services Administration. (2016). *Cast iron: Characteristics, uses and problems*. GSA.gov. https://www.gsa.gov/real-estate/historic-preservation/historic-preservation-policy-tools/preservation-tools-resources/technical-procedures/cast-iron-characteristics-uses-and-problems

Yuantai Steel Pipe. (2024). *Metallographic analysis and comparison of ferrite, cementite, pearlite, austenite, martensite, bainite, ledeburite, and Widmannstatten structure*. https://www.yuantaisteelpipe.com/blog/Metallographic-analysis-and-comparison-of-ferrite-cementite-pearlite-austenite-martensite-bainite-ledeburite-and-Widmannstatten-structure_b626

DEPARTMENT OF MECHANICAL ENGINEERING
DIVISION OF MATERIALS AND MANUFACTURE
CHALMERS UNIVERSITY OF TECHNOLOGY
Gothenburg, Sweden 2026
www.chalmers.se

CHALMERS